A chronological and palaeoenvironmental re-evaluation of two loess-palaeosol records in the northern Harz foreland, Germany, based on innovative modelling tools

CHRISTOPH SCHMIDT (iD), CHRISTIAN ZEEDEN (iD), LYDIA KRAUß (iD), FRANK LEHMKUHL (iD) AND LUDWIG ZÖLLER (iD)

The continuing development of analytical methods for investigating sedimentary records calls for iterative re-examination of existing data sets obtained on loess-palaeosol sequences (LPS) as archives of palaeoenvironmental change. Here, we re-investigate two LPS (Hecklingen, Zilly) in the northern Harz foreland, Germany, being of interest due to their proximity to the Scandinavian Ice Sheet (SIS) and the position between oceanic climatic influence further west and continental influence towards the east. First, we established new quartz OSL and polymineral IRSL chronologies. Both methods show concordant ages in the upper part of the Hecklingen profile (~20–40 ka), but in the lower part IRSL underestimates OSL ages by up to ~15 ka for the period 40–60 ka. Interpretations hence refer to the OSL data set. Second, we applied Bayesian age-depth modelling to data sets from Hecklingen to resolve inversions in the original ages, also reducing averaged 1σ uncertainty by ~19% (OSL) and ~12% (IRSL). Modelled chronologies point out phases of increased (MIS 2, early MIS 3) and reduced (middle and late MIS 3) sedimentation, but interpretation of numerical rates is problematic because of intense erosion and slope wash particularly during MIS 3. Finally, previously obtained grain-size data were re-investigated by end member modelling analyses. Three fundamental grain-size distributions (loadings) explain the measured data sets and offer information on intensity and – combined with modelled OSL ages – timing of geomorphic processes. We interpret the loadings to represent (i) primary loess accumulation, (ii) postdepositional pedogenesis and/or input of aeolian fine fractions, and (iii) input of coarse aeolian material and/or slope wash. The applied modelling tools facilitate detailed understanding of site-formation through time, allowing us to correlate a strong peak in mean grain size at ~26–24 ka to the maximum extent of the SIS and increased influence of easterly winds.

Christoph Schmidt (christoph.schmidt@unil.ch), Chair of Geomorphology & BayCEER, University of Bayreuth, Universitätsstr. 30, Bayreuth 95440, Germany and Institute of Earth Surface Dynamics, University of Lausanne, Géopolis, Lausanne 1015, Switzerland; Christian Zeeden, Leibniz Institute for Applied Geophysics, Stilleweg 2, Hannover 30655, Germany; Lydia Krauß, Department of Geography, RWTH Aachen University, Wüllnerstr. 5b, Aachen 52056, Germany and Geomorphology and Soil Science, TUM Technical University of Munich, Hans-Carl-v.-Carlowitz-Platz 2, Freising-Weihenstephan 85354, Germany; Frank Lehmkuhl, RWTH Aachen University, Wüllnerstr. 5b, Aachen 52056, Germany; Ludwig Zöller, Chair of Geomorphology & BayCEER, University of Bayreuth, Universitätsstr. 30, Bayreuth 95440, Germany; received 6th June 2020, accepted 28th December 2020.

The northern Harz foreland, Germany, is close to the former southern border of the Weichselian Scandinavian Ice Sheet (SIS) and comprises large areas covered by loess. Research on the distribution and characteristics of loess-palaeosol sequences (LPS) in the region is thus of special interest for reconstructing Pleistocene palaeoclimatic conditions in ice-marginal environments (Reinecke 2006; Lehmkuhl *et al.* 2016). Atmospheric dust dynamics, palaeowind velocity and change in main palaeowind directions during individual phases of a glacial cycle in the vicinity of the SIS margin can be retrieved from LPS proxy data in that area. As such, the Harz foreland also represents an essential link for comparative Late Pleistocene palaeoenvironmental reconstructions from the western and oceanic parts of Europe to the more continental areas in eastern Europe.

Furthermore, due to rain-shadow effects of the Harz Mountains the eastern part of the northern foreland only receives modern precipitation ≤500 mm a^{-1} (Döring 2004; Fig. 1). This small-scale gradient from an oceanic climate in the west to a continental one in the east offers the possibility to study the environmental effects of such variations for the past.

However, most studies north of the Harz Mountains focused on the transitional zone and its silt- and sand-sized Weichselian aeolian sediments (Poser 1951; Brosche & Walther 1978; Gehrt 1994; Gehrt & Hagedorn 1996; Hilgers *et al.* 2001). One of the few recent investigations on LPS in the northern Harz foreland by Reinecke (2006) addressed two LPS outcrops near the villages Hecklingen and Zilly (Fig. 1). While the Zilly profile preserves only Lateglacial loess, the LPS at Hecklingen encompasses a more continuous record back to MIS 3 at least (Reinecke 2006). This is in stark contrast to observations from Saxony, Poland and western Ukraine, indicating a strong erosional phase causing large depositional gaps in most places (e.g. between ~65 and ~35 ka; Jary & Ciszek 2013; Meszner *et al.* 2013).

Krauß *et al.* (2016) re-investigated the LPS at Hecklingen and Zilly, applying a multi-proxy approach (grain
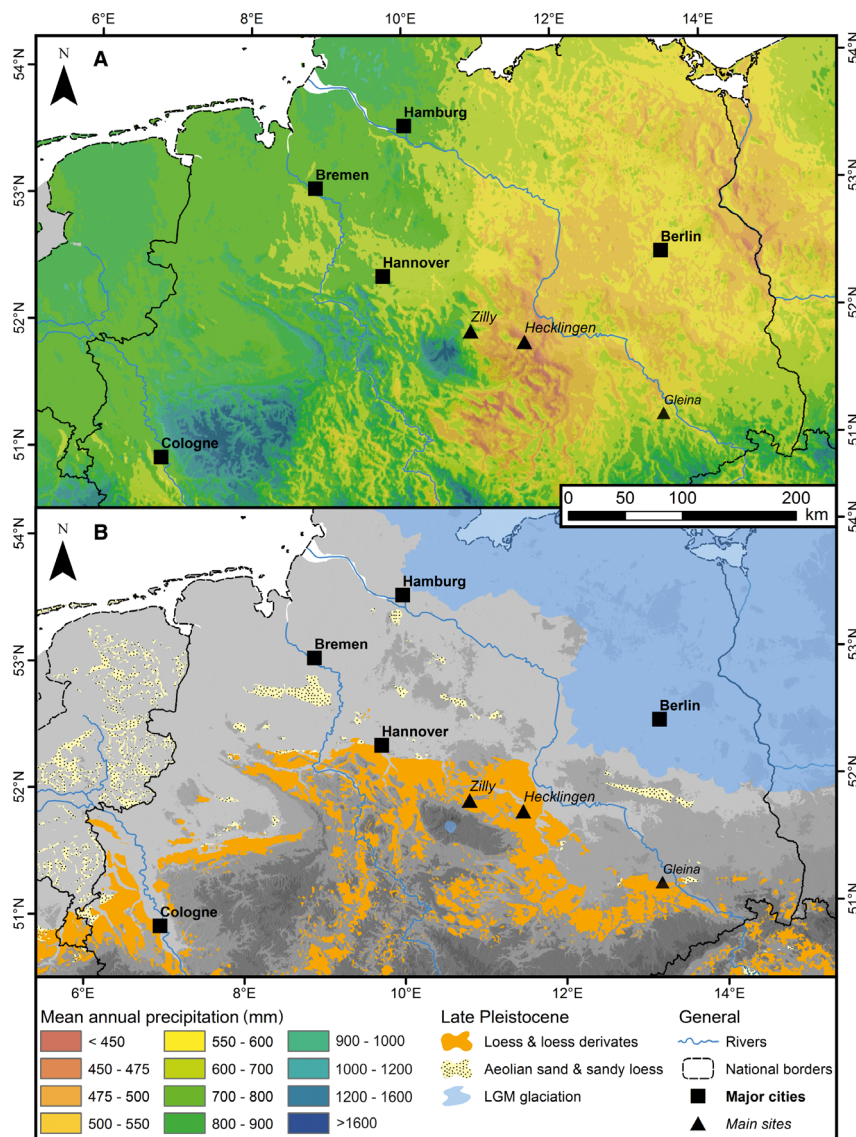
Fig. 1. A. Annual precipitation in northern Germany. Data adapted from Karger *et al.* (2017). B. Glacial extent during the Last Glacial Maximum (modified from Ehlers *et al.* 2011). Study sites Zilly and Hecklingen (Gleina for comparison) in the North European loess belt. The loess distribution is according to Lehmkuhl *et al.* (2018). In the Netherlands the data are based on the geological map (scale 1:600 000; Zagwijn & Van Staalduinen 1975) and for Poland (Dobrzański *et al.* 1974) national soil maps were digitized.

size, geochemical (XRF, CNS), colour and rock magnetic analyses). For chronological correlation, they used re-calculated infrared stimulated luminescence (IRSL) ages by Reinecke (2006). However, this study raised several questions on the chronology of different layers: for instance, data of the assumed MIS 3 soil complex indicate more than one phase of soil development and intercalated erosional events (Krauß *et al.* 2016), implying that the period displayed in the preserved material likely exceeds 10 ka in Hecklingen (Blume *et al.* 2016). However, IRSL ages show an inversion between the layer below and the assumed MIS 3 complex and therefore only a short period available for pedogenesis. Additionally, Krauß *et al.* (2016) obtained data indicating wind

direction changes towards stronger easterly winds during the local Last Glacial Maximum (lLGM). They further assumed age underestimation of Reinecke's (2006) ages by 4–6 ka (Frechen & Schirmer 2011; Schmidt *et al.* 2011; Zens *et al.* 2017) and a timing of the LGM from 26.5 to 19.0 ka (Clark *et al.* 2009). These discrepancies and assumptions call for further reliable chronometric control on loess deposition. Moreover, previous IRSL ages were not corrected for anomalous fading, an effect causing age underestimation (e.g. Wintle 1973; Huntley & Lamothe 2001).

When sedimentation rates as proxies of dust activity and loess depositional dynamics are to be inferred from chronostratigraphical data, age inversions – although to

be expected for geomorphological and statistical reasons and a common phenomenon – pose major problems in interpretation. The IRSL ages by Krauß *et al.* (2016) contain such an age inversion in the lower part of the Hecklingen profile. Here, Bayesian age-depth modelling represents a viable tool because (i) age inversions do not exist in modelled data and (ii) uncertainty can be reduced considerably. The method was first applied to radiocarbon dates mostly in archaeological contexts (e.g. Buck *et al.* 1991, 1996; Bronk Ramsey 1995), but comparatively few methodological studies on Bayesian modelling of stratigraphically ordered luminescence samples (Rhodes *et al.* 2003; Millard 2004; Combès & Philippe 2017; Zeeden *et al.* 2018; Lanos & Dufresne 2019) and only a small number of applied investigations exist (Noppradit *et al.* 2018; Perić *et al.* 2019; Fenn *et al.* 2020). Such age-depth modelling, however, can potentially resolve the problem of a too short period of pedogenesis of the MIS 3 soil complex at Hecklingen, resulting from the age inversion in the previous IRSL data set.

Another constraint inherent to the proxy data by Krauß *et al.* (2016) is the selection of specific grain-size fractions taken to be indicative of source area, transport pathway, intensity and characteristics of aeolian geomorphic as well as (post)depositional processes. In general, grain size is a sensitive proxy of the listed factors (e.g. Doeglas 1968; Vandenberghe 2013; Újvári *et al.* 2016; Vandenberghe *et al.* 2018) and the ISO 14688 standard separation into sand, silt and clay based on the logical mathematical classification of Atterberg (1905) is often used to describe sediment characteristics including transport energies and modes (Assallay *et al.* 1998; Blott & Pye 2012). However, natural processes do not always follow such imposed categorizations, and the reconstruction of source area and driving transport regimes should thus avoid predefined grain-size classifications. Moreover, grain-size populations characteristic for the source material and transport process can be multi-modal or overlapping, further complicating an interpretation based on fixed grain-size classes (Dietze & Dietze 2019). Deterministic (e.g. Gan & Scholz 2017) and robust (probabilistic; e.g. Dietze *et al.* 2012; Paterson & Heslop 2015; Dietze & Dietze 2016) end member modelling analyses (EMMA) allow extraction of informative and unbiased subpopulations from bulk grain-size data, indicative of involved materials, transport modes and postdepositional alteration. It seems therefore worthwhile applying EMMA to the grain-size data by Krauß *et al.* (2016) for the Hecklingen and Zilly LPS to explore if unconstrained and unbiased extraction of grain-size subpopulations allows for new findings beyond existing interpretations on palaeowind characteristics.

The aim of this paper is to tackle the mentioned challenges and inconsistencies by producing new quartz OSL and polymineral IRSL ages for the LPS at Hecklingen and Zilly. The new chronometric data will allow re-evaluation of part of the palaeoclimate proxy data by Krauß *et al.* (2016) and resolution of the discrepancies arising with their IRSL data set. We apply Bayesian age-depth modelling to circumvent age inversions and increase the precision of the luminescence chronology of the Hecklingen profile. In addition, we perform EMMA with the grain-size data previously obtained for both sites and place median and modelled grain-size data as a proxy for palaeowind velocity onto the modelled OSL chronology to estimate sedimentation rates for the Hecklingen record. Finally, we re-evaluate the previous chronometric and proxy data for the study sites and discuss the implications within the wider context of dust flux and palaeoenvironments in the North European loess belt.

Study sites and previous research

The profiles Hecklingen (latitude 51°50.451′N, longitude 11°31.580′E, altitude 106 m a.s.l.) and Zilly (51°56.280′N, 10°50.643′E, 182 m a.s.l.) are located in the northern and northeastern Harz foreland in Germany, respectively (Fig. 1). Rain-shadow effects of the Harz Mountains influence the current climate conditions in this region, whereas in the west a stronger suboceanic influence is registered (Fig. 1; Haase *et al.* 1970; Döring 2004; Reinecke 2006; Fabig 2007; Krauß *et al.* 2013, 2016). Pleistocene deposits within the northern Harz foreland are mainly loose sediments and vary in thickness, composition and sedimentary origin. The loess-covered areas are part of the northern European loess belt (Lehmkuhl *et al.* 2016).

During the Elsterian and Saalian glacial cycles, the SIS covered the northern Harz foreland, and during the last glacial this region belonged to the periglacial area with the ice margin further north (Fig. 1). Therefore, preserved loess sediments only date back to the last glacial period and form a 40–50 km wide belt of Weichselian loess (Fig. 1). Generally, the loess cover rarely exceeds 2.5 m of thickness.

According to Krauß *et al.* (2016), the Hecklingen section (Fig. 2, left) comprises from top to bottom a grey tundra gley (supposedly MIS 4) at the base followed by a loess layer and a truncated soil (MIS 3). This is overlain by a presumably MIS 3 soil complex of 2 m thickness and a stony loess layer containing large amounts of gravel, followed by a ~4-m-thick loess complex with four intercalated tundra gley soils (Gelic Cryosols, MIS 2). The uppermost 1.2 m represents the recent soil complex.

In the Zilly section (Fig. 2, right), a ~4-m-thick loess complex with three intercalated tundra gleys (MIS 2) is preserved. The uppermost 1.2 m of the profile represents the recent soil complex. Based on proxy data, both profiles were divided into different units (units I to VI in Hecklingen and units I to III in Zilly), as displayed in Fig. 2 and explained in detail in Krauß *et al.* (2016).
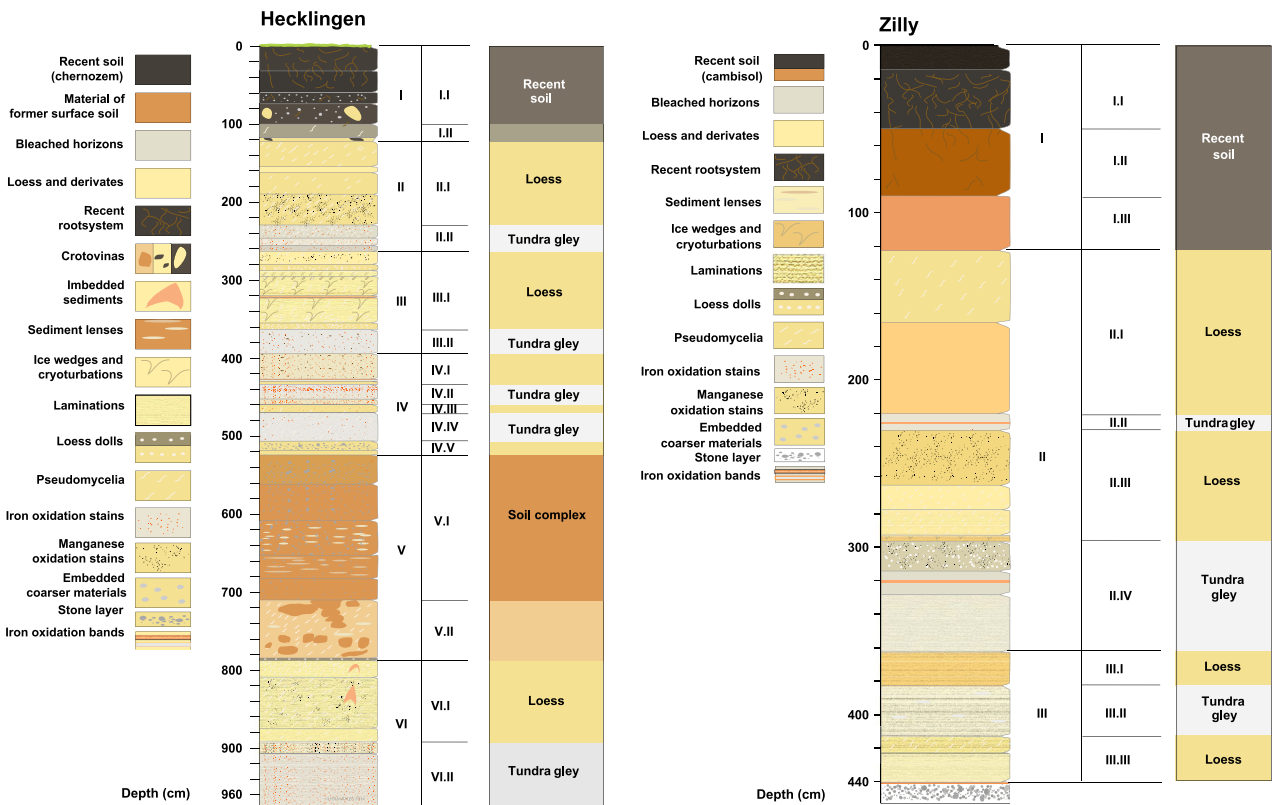
Fig. 2. Stratigraphy and lithological description of the loess-palaeosol sequences of Hecklingen and Zilly.

Photographs of the cleaned profiles are compiled in Figs S1–S5.

In 2003/2004, A. Hilgers (University of Cologne) performed IRSL measurements for polymineral silt-sized samples from the Hecklingen and Zilly sections. Since Reinecke (2006) published these ages without additional information concerning the dating procedure, this data set was re-evaluated by Krauß *et al.* (2016) using different signal integration intervals and statistical processing. Main procedural differences between the previous IRSL data set (Krauß *et al.* 2016) and the here presented new polymineral IRSL ages refer to the preheat conditions (270 °C for 10 s vs. 270 °C for 120 s), the IRSL reading temperature (50 vs. 125 °C), an inserted 'hot-bleach' at the end of each SAR cycle (only new data set) and the methods used for dose rate assessment (γ-ray spectrometry vs. thick-source α-counting and ICP-OES). A summary of the IRSL ages by Krauß *et al.* (2016) along with relevant dose rate data is given in Table 1.

Material and methods

Luminescence dating

During fieldwork, neither suitable organic or carbon-bearing material for radiocarbon dating nor tephra was found that could provide numeric or relative age control for the Hecklingen and Zilly LPS. Therefore, in 2014 eight new luminescence samples from the Hecklingen profile and two new luminescence samples from the Zilly profile were taken by hammering steel tubes into the cleaned profile walls. Dose rate samples were taken from the matrix in the vicinity of the luminescence sampling holes relevant for the contribution of γ-radiation. Unfortunately, it was not possible to obtain samples from identical sampling locations as used for the previous IRSL data set (Reinecke 2006; Krauß *et al.* 2016) due to erosion of the profile sections in between the two sampling campaigns.

The preparation of luminescence samples was conducted following common procedures for the luminescence fine grain (~4–11 μm) technique (Berger *et al.* 1980; refer to Data S1 in Supporting Information for details, also on instrumentation for luminescence measurements).

For OSL equivalent dose (D_e) determination on quartz, a single aliquot regeneration (SAR) protocol (Murray & Wintle 2000; Table 2) was applied, using the signal integrated from the first 0.6 s of the decay curve minus a background averaged from the last 7.5 s. The dose points (signal integral vs. dose) were fitted with a single saturating exponential function. The D_e of polymineral samples was determined using a modified

Table 1. Summary of IRSL ages as published by Krauß *et al.* (2016; re-calculated from Reinecke 2006). Dose rate calculations are based on radionuclide concentrations from laboratory γ-ray spectrometry and equivalent dose (D_e) determination on single aliquot regeneration (SAR) measurements following Murray & Wintle (2000) and Wallinga *et al.* (2000). Main differences between this previous approach and our new data set include the preheat conditions (270 °C for 10 s vs. 270 °C for 120 s), the IRSL reading temperature (50 vs. 125 °C), an inserted 'hot-bleach' at the end of each SAR cycle (only new data set) and the methods used for dose rate assessment (γ-ray spectrometry vs. thick-source α-counting and ICP-OES).

Laboratory code	Sample code	Depth (m)	n^1	Recycling ratio	D_e (Gy)	K (wt.%)	Th (ppm)	U (ppm)	H₂O content meas. (wt.%)	H₂O content (wt.%)	Total $\dot{D}$ (Gy ka⁻¹)	IRSL age (ka)
C-L1305	HCK-1	1.40	4/4	0.96±0.01	56.0±3.0	1.41±0.03	7.73±0.58	2.30±0.13	5	12.5±5	3.16±0.18	17.8±1.4
C-L1306	HCK-2	2.35	6/6	0.96±0.01	79.4±4.2	1.50±0.03	9.30±0.51	2.50±0.21	13	12.5±5	3.46±0.20	22.9±1.8
C-L1307	HCK-3	3.55	6/6	0.96±0.02	79.3±4.2	1.52±0.03	9.64±0.59	2.41±0.13	14	12.5±5	3.44±0.19	23.1±1.8
C-L1308	HCK-4	5.25	6/6	0.91±0.02	166.9±11.1	1.47±0.03	8.76±0.54	2.22±0.09	13	12.5±5	3.24±0.18	51.5±4.5
C-L1309	HCK-5	7.75	6/6	0.94±0.01	150.6±8.1	1.42±0.03	8.06±0.46	2.15±0.18	11	12.5±5	3.11±0.18	48.5±3.8
C-L1310	HCK-6	8.55	6/6	0.93±0.01	157.7±8.5	1.28±0.03	6.62±0.37	1.57±0.12	13	12.5±5	2.55±0.14	61.9±4.7
C-L1386	ZIL-1	0.80	6/6	0.95±0.02	55.3±2.9	1.79±0.04	9.00±0.50	2.28±0.28	3	12.5±5	3.66±0.20	15.1±1.1
C-L1387	ZIL-2	1.35	6/6	0.95±0.02	50.4±2.7	1.59±0.03	7.92±0.61	2.20±0.10	3	12.5±5	3.32±0.18	15.2±1.1
C-L1388	ZIL-3	2.28	6/6	0.96±0.01	50.1±2.6	1.51±0.03	7.98±0.52	2.28±0.08	2	12.5±5	3.27±0.18	15.4±1.2
C-L1389	ZIL-4	2.44	6/6	0.94±0.01	54.1±2.8	1.55±0.03	8.61±0.53	2.44±0.20	1	12.5±5	3.42±0.19	15.8±1.2

[1] Accepted in relation to measured number of aliquots.

IRSL SAR protocol, building on previous experience by Preusser (2003), Rother *et al.* (2010) and Faust *et al.* (2015). While employing a preheat at 270 °C for 120 s prior to IRSL readout for 300 s at 90% LED power and 125 °C, it additionally allows for a resting period of 20 min between preheat and IR stimulation (Table 2). This pause is intended to minimize anomalous fading (e.g. Wallinga *et al.* 2001; Balescu *et al.* 2003), which frequently causes D_e underestimation of feldspar-bearing samples (Wintle 1973). Except for sample BT1543, a 'hot-bleach' of 300 s IR stimulation at 270 °C was inserted at the end of each SAR cycle to reduce the signal carry-over to the next cycle. The dose points, obtained from the signal integral of the first 2 s of the IRSL decay curve corrected for a background averaged from the last 50 s, were fitted with a single saturating exponential function. For details on fading and residual dose experiments, see Data S1, Table S1 and Fig. S6.

To find optimal preheat conditions and a thermally stable signal, OSL preheat plateau tests (PPT; BT1534, BT1537, BT1540) and dose recovery tests (DRT; OSL: BT1534, BT1537, BT1541; IRSL: BT1537) (e.g. Murray & Wintle 2003) were conducted in the range 180–260 °C, while preheat and cutheat temperatures were identical (for further details refer to Data S1). All D_e values were calculated with the Analyst software (version 4.31.9; Duller 2015) and employing the central age model (CAM; Galbraith *et al.* 1999). Aliquots not fulfilling the following criteria were rejected: (i) initial signal >3σ above background (with σ being the standard deviation of the background), (ii) test dose error ≤10%, (iii) recuperation <5%, (iv) recycling ratio between 0.9 and 1.1, and (v) IR depletion ratio differs <3% from unity (OSL only).

Dose rate samples were analysed by thick-source α-counting (Aitken 1985; Zöller & Pernicka 1989) and ICP-OES to quantify U, Th and K concentrations. Prior to radioelement analyses, sediment samples were homogenized to ensure that minute, cm-scale variations in radioactivity were averaged. Moisture estimation was mainly based on measured water contents of the samples but includes an additional absolute uncertainty of 5% to take into account moisture fluctuations during burial time. Samples from the Zilly site showed unusually low water content of 1%, certainly not reflecting a representative value for the burial period. We therefore adopted an assumed moisture content of 12.5±5% for the two samples. The sediment cover was estimated to 50% of the present value for cosmic dose rate calculation. Following Mauz *et al.* (2006) and Schmidt *et al.* (2018), an *a*-value of 0.030±0.003 (OSL) or 0.08±0.02 (IRSL) was assumed for α-dose rate calculation. Dose rates and luminescence ages were calculated with DRAC (v1.2; Durcan *et al.* 2015) using conversion factors from Guérin *et al.* (2011), α-attenuation factors from Brennan *et al.* (1991) and β-attenuation factors from Guérin *et al.* (2012).

Table 2. OSL and IRSL protocols used to determine the equivalent dose. Step 1 is skipped for the first cycle (measuring the natural OSL or IRSL signal).

OSL			IRSL		
Step	Procedure	Signal	Step	Procedure	Signal
1	Irradiation with regeneration dose		1	Irradiation with regeneration dose	
2	Preheat at 220 °C for 10 s		2	Preheat at 270 °C for 120 s	
3	OSL at 125 °C for 40 s	L_x	3	Pause for 20 min	
4	Irradiation with test dose		4	IRSL at 125 °C for 300 s	L_x
5	Cutheat to 220 °C		5	Irradiation with test dose	
6	OSL at 125 °C for 40 s	T_x	6	Preheat at 270 °C for 120 s	
7	Return to step 1		7	Pause for 20 min	
			8	IRSL at 125 °C for 300 s	T_x
			9	IRSL at 270 °C for 300 s	
			10	Return to step 1	

Bayesian age-depth modelling

Age-depth modelling was done using the ADMin method (Zeeden *et al.* 2018), which is especially tailored for luminescence data. The age-depth model inferred from the new OSL ages was then taken to place data on an age scale through linear interpolation between modelled ages. To this aim, the function tune() in the R (R Core Team 2020) package 'astrochron' (v0.9; Meyers 2014) was used. For comparative purposes, the same procedure was performed with the grain-size data in conjunction with the 'old' IRSL data set by Krauß *et al.* (2016) to reveal the changes in interpretation associated with the new OSL chronology.

Unmixing grain-size data by end member modelling analyses

Details on raw grain-size data generation are given in Krauß *et al.* (2016). The R package 'EMMAgeo' (Dietze *et al.* 2012; Dietze & Dietze 2016, 2019) served to extract grain-size populations representing most closely source material, pedologic and geomorphic processes. Initially, the number of useful end members was established, thereafter end member analysis was performed without specifying weight transform limits or enforcing specific sums for scaling. However, these parameters have little influence over the result and different settings would not result in different interpretations.

Results

Luminescence dating

The OSL signal of all samples decays to instrumental background level within <10 s (Fig. 3A). Hence, it can be assumed that the signal integral used to construct the dose-response curve is dominated by the thermally stable fast component. Dose-response curves can be well fitted with a single saturating exponential function (Fig. 3A), while the characteristic dose saturation values D_0 (Wintle

& Murray 2006) vary between ~100 and ~150 Gy. PPTs indicate that for temperatures of 180–260 °C the SAR D_e values of samples BT1534, BT1537 and BT1540 do not vary significantly (Fig. 3B). A preheat temperature of 220 °C (middle of the preheat plateau) was therefore adopted for the DRTs, which were successful with a dose reproducibility better than 2% for sample BT1534 (given dose 52.4 Gy), while a slight tendency for dose under-estimation becomes apparent for sample BT1537 (7% underestimation for 196.3 Gy given dose). The recovered dose of sample BT1541 is 11% lower than the given dose of 130.9 Gy (Table 3). With a recovery ratio of 0.98±0.01 a given dose of 179.8 Gy could be accurately reproduced for polymineral sample BT1537 with the IRSL SAR protocol. A residual dose of 6.7±0.4 Gy was subtracted from all IRSL D_e values and considered in the DRT.

IRSL fading tests indicate generally negligible to low fading rates for all measured samples. While for samples BT1535 and BT1543 all of the five aliquots yielded *g*-values not significantly different from zero, results from sample BT1539 gave *g*-values between 0.51±1.50 and 2.50±1.44% per decade. Averaged *g*-values of samples BT1535, BT1539 and BT1543 amount to 0.62±0.65, 1.37±0.72 and 0.67±0.39% per decade, respectively (*n* = 5 in all cases, uncertainty given as 1σ standard deviation; Table S1 and Fig. S6). However, due to the additional resting period of 20 min between irradiation and measurement an additional 'fading' time delay of only ~1.5 decades could be achieved. Fading correction was applied to all IRSL ages using the average of all measured *g*-values (0.89±0.14% per decade) and the function calc_FadingCorr() in the R package 'Lumines-cence' (Kreutzer *et al.* 2012a; Kreutzer 2020), following the approach by Huntley & Lamothe (2001). The IRSL ages corrected for fading and residual dose are statisti-cally indistinguishable from the uncorrected IRSL ages.

Results from radioelement analyses, moisture deter-mination and cosmic dose rate calculation are compiled in Table 4, while D_e values, total dose rates and ages are summarized in Table 5. A correlative overview of the new

OSL and IRSL ages is shown in Fig. 4A for the Hecklingen profile, and a summary of all luminescence ages along with their positions in the Hecklingen and Zilly sections is given in Fig. 5.

In Hecklingen, OSL D_e values and ages increase with depth from 75.0 ± 0.7 Gy (21.9 ± 1.4 ka) to 205.8 ± 2.8 Gy (59.9 ± 3.8 ka), except for two ages being slightly younger than the adjacent upper samples (BT1539 at 4.70 m and BT1535 at 9.35 m). IRSL data yields D_e values between 69.8 ± 4.5 and 178.4 ± 17.1 Gy and fading-corrected ages in the range 19–49 ka. Except for sample BT1540, OSL and IRSL chronologies agree within uncertainty up to ~40 ka (~6 m depth; units II.I to V.I), while OSL ages are generally older than IRSL ages. Below this depth, IRSL yields consistently younger ages for samples BT1536 and BT1537, as compared to OSL. The stratigraphically lowermost sample in Hecklingen produced OSL and IRSL ages overlapping again at 1σ (52.8 ± 3.3 and 49.1 ± 5.6 ka, respectively). Both OSL and IRSL ages do not significantly increase with depth below ~7 m, and, unlike the OSL chronology, the IRSL data set does not contain significant age inversions. Considering recent methodological investigations (see further discussion below), OSL and IRSL ages in the lower part of the profile might suffer from underestimation.

Bayesian age-depth modelling

Calculated probability density functions (PDFs) of random uncertainties in luminescence ages for both the OSL and IRSL data sets from the Hecklingen profile are plotted in Fig. 6. They visualize the relative degree of random uncertainty that is able to explain the observed age inversions in the data set (Zeeden *et al.* 2018). Due to the high number of age inversions in the OSL data set, a high random uncertainty must be assigned, and the PDF curve starts to rise only above ~50% random uncertainty. By contrast, the IRSL data set can be explained reasonably well with random uncertainties starting from 10–20%. A comparison of original and modelled ages along with their 1σ uncertainties is shown in Fig. 4B and Table 5.

The derivation of sedimentation rates and the re-interpretation of palaeoenvironmental proxy data will, however, be based on modelled OSL ages alone. The reason is that signal fading has not been reported for OSL from non-volcanic quartz but cannot be entirely excluded as a reason for the underestimated IRSL ages from the lower part of the Hecklingen profile.

Sedimentation rates inferred from the modelled OSL ages

While it is not possible to derive trends in sedimentation rate from the original ('un-modelled') OSL or previous
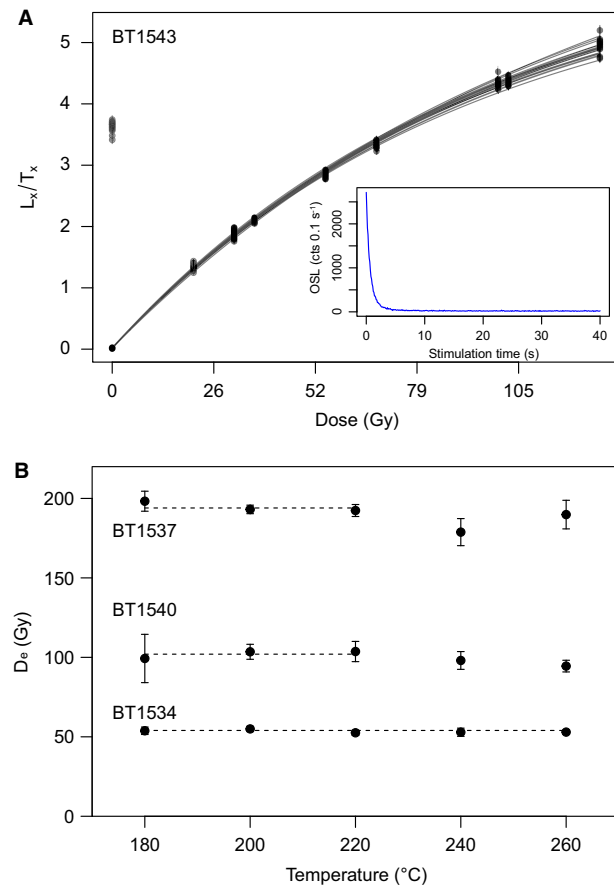

Fig. 3. A. Dose-response curves of 21 aliquots of sample BT1543, approximated by single saturating exponential functions. The inset shows a typical natural OSL decay curve of the same sample. B. Results of the preheat plateau test for samples BT1534, BT1537 and BT1540. The dashed line indicates the preheat plateau. Data points represent the average and standard deviation of three (BT1537) or four aliquots (BT1534 and BT1540).

IRSL (Krauß *et al.* 2016) ages, the modelled OSL ages suggest three intervals of rather stable mean sedimentation rates for the Hecklingen LPS (Fig. 4B). While generally the delineation of changes in sedimentation rate from age-depth plots has an inherently subjective element to it, the changes in dust accumulation rates for the Hecklingen site can be clearly constrained to the lower and upper boundary of the MIS 3 soil complex. Until ~54 ka, sedimentation rates are in the order of

Table 3. Results of the dose recovery test for the silt-sized quartz and polymineral samples measured by OSL and IRSL. Uncertainties are given as 1σ standard error.

Sample	Method	Given dose (Gy)	Recovered dose (Gy)	Ratio
BT1534	OSL	52.4	51.5 ± 1.4	0.98 ± 0.02
BT1537	OSL	196.3	181.8 ± 1.1	0.93 ± 0.01
BT1541	OSL	130.9	116.5 ± 2.0	0.89 ± 0.01
BT1537	IRSL	179.8	177.4 ± 1.9	0.98 ± 0.01

Table 4. Results from radioelement analyses, moisture content and cosmic dose rate for the luminescence samples from Hecklingen and Zilly. Note that all analytical values and are given with 1σ uncertainty.

Laboratory code	Field code	Depth (m)	K (wt.%)	Th (µg g^{-1})	U (µg g^{-1})	H$_2$O content meas. (wt.%)	H$_2$O content (wt.%)	Cosmic $\dot{D}$ (Gy ka^{-1})
BT1543	HCK1_10	2.00	1.80±0.18	9.13±0.94	3.04±0.28	5	12.5±5	0.187±0.019
BT1542	HCK1_9	2.40	1.78±0.18	7.15±0.82	3.26±0.25	10	12.5±5	0.182±0.018
BT1540	HCK1_6	4.10	1.78±0.18	7.75±0.87	3.63±0.27	6	12.5±5	0.164±0.016
BT1539	HCK1_5	4.70	1.90±0.19	8.85±0.92	3.56±0.28	12	12.5±5	0.158±0.016
BT1538	HCK1_4	6.00	1.60±0.16	9.22±0.93	3.18±0.28	11	12.5±5	0.147±0.015
BT1537	HCK1_3	7.75	1.54±0.15	8.70±0.92	3.48±0.28	6	12.5±5	0.132±0.013
BT1536	HCK1_2	8.50	1.65±0.17	9.42±0.97	3.71±0.29	7	12.5±5	0.127±0.013
BT1535	HCK1_1	9.35	1.58±0.16	9.25±0.95	3.58±0.29	10	12.5±5	0.121±0.012
BT1534	Zil1_3	1.30	1.97±0.20	8.76±0.98	2.88±0.30	1	12.5±5	0.204±0.020
BT1533	Zil1_1	2.40	1.82±0.18	8.88±1.02	3.41±0.31	1	12.5±5	0.185±0.019

0.44 m ka^{-1}. From ~54–28 ka, sedimentation rates are lower and at 0.11 m ka^{-1} on average. Thereafter, they increase again to a level of ~0.45 m ka^{-1}. Note that the model does not make any initial assumptions on the sedimentation process and that it cannot differentiate between intervals including erosion and those characterized by low sedimentation rates. These reservations apply in particular to units V.I and V.II, where phases of soil erosion and subsequent deposition of soil sediment were inferred from lithology and geochemical data (Ba/Sr and Rb/Sr ratios; Krauß *et al.* 2016). In comparison to LPS formed at plateau positions, the topographic situation at Hecklingen may favour distortions of the calculated sedimentation rates due to erosion and/or accumulation of material from further upslope. This should be kept in mind when assessing the validity of such sedimentation rates and contrasting them with values obtained at LPS that formed in different genetic settings.

End member modelling analysis (EMMA) of grain-size data

Applying the EMMAgeo algorithm results in three multi-modal grain-size populations ('loadings') as the best description of the grain-size data set of the Hecklingen profile, characterized by maxima at ~25, ~35 and ~400 µm. The coarsest loading has additional peaks at ~55 and ~200 µm of roughly the same relative intensity. The EMMAgeo algorithm suggested two to seven loadings for the Zilly grain-size data set, but for reasons of consistency we decided to use three loadings here as well. Maxima of the loadings are at ~15, ~30 and ~50 µm. Generally, the loadings obtained for the two sites show two to three additional sub-modes towards larger grain-size values (Fig. 7A, B). The end member scores as the relative contribution of each loading are shown against sampling depth for the two profiles in Fig. 7C, D. Grain size class-wise explained variance amounts to 74 and 77% for Hecklingen and Zilly, and the sample-wise explained variation averages to 89 and 83%, respectively (Fig. S7). Figures S8 and S9 show the modelled loadings and scores at both sites along with the 'classically' obtained

grain-size contributions (sand, silt, clay). A more detailed description of the modelled grain-size data sets will be provided in the next section when they are referenced to age by placing them onto the Bayesian age-depth model.

Placing proxy data onto the Bayesian age model

To demonstrate the effect of Bayesian age-depth modelling on the interpretation of sedimentary proxy data for palaeoenvironmental reconstruction, we first compare the old 'linear IRSL' with the new 'Bayesian OSL' chronology for the proxy 'mean grain size' (see Krauß *et al.* 2016, 2017 for the data set). The 'Bayesian OSL' model in combination with the mean grain size shows a shift compared to the 'linear IRSL' model (Fig. 8) and two main changes in the timing of enhanced mean grain size. (i) The increased mean grain size documented for the MIS 3 soil complex is extended time-wise. While according to the 'linear IRSL' age model grain size reduces to values around 30–40 µm at ~38–37 ka and thus long before termination of MIS 3, the new age model implies a roughly contemporaneous reduction of grain size with the end of MIS 3 at ~29 ka. (ii) The threefold and strong peak in mean grain size during MIS 2 is 'squeezed' time-wise according to the new age model, approximately by a factor of 3. It now represents a comparatively short period between ~26 and ~24 ka.

The results from EMMA as placed onto the Bayesian OSL age model are shown in Fig. 9 for the three loadings derived for the Hecklingen profile. The most characteristic feature is the drop to zero of loading 1 during MIS 2, which is considerably shortened in duration with the new age model (from ~4 to ~1–2 ka). Furthermore, the peak in relative contribution of loading 1 is shifted from ~36–34 ka in late MIS 3 to ~28–27 ka in early MIS 2 (Fig. 9A). The period of complete absence of loading 2 in the data set is extended time-wise with the new age model from a duration of ~15 to ~20 ka and now reaches into early MIS 2, while it ended at ~35 ka (MIS 3) with the old age model. Additionally, the four peaks in relative abundance of loading 3 previously occurring between

Table 5. Results from OSL and IRSL measurements and calculated ages. The OSL and IRSL ages as resulting from Bayesian age-depth modelling are shown for comparison in the last column. Note that all dose rates and luminescence ages are given with 1σ uncertainty.

Laboratory code	Field code	Depth (m)	OSL n[1]	Recycling ratio	D_e[2] (Gy)	Total $\dot{D}$ (Gy ka⁻¹)	Age (ka)	Modelled age (ka)	IRSL n[1]	Recycling ratio	D_e[2] (Gy)	Total $\dot{D}$ (Gy ka⁻¹)	Age (ka)	Fading-corr. age (ka)	Modelled age (ka)
BT1543	HCK1_10	2.00	21/21	1.03±0.04	75.0±0.7	3.419±0.190	21.9±1.4	21.6±1.3	10/10	1.03±0.04	69.8±4.5	3.966±0.218	17.6±1.5	18.9±1.6	18.9±1.7
BT1542	HCK1_9	2.40	23/24	1.03±0.03	78.0±0.7	3.296±0.185	23.7±1.5	23.9±1.3	6/10	1.07±0.02	80.3±7.6	3.812±0.210	21.1±2.3	22.6±2.5	22.6±2.3
BT1540	HCK1_6	4.10	24/24	1.01±0.04	105.3±1.2	3.431±0.189	30.7±2.0	26.9±1.5	10/10	1.00±0.02	96.1±5.7	4.000±0.219	24.0±1.9	25.8±2.1	25.2±1.8
BT1539	HCK1_5	4.70	20/20	1.04±0.03	90.9±1.1	3.604±0.199	25.2±1.6	27.7±1.4	10/10	1.01±0.03	99.7±6.5	4.196±0.230	23.8±2.0	25.5±2.2	26.4±2.0
BT1538	HCK1_4	6.00	24/24	1.03±0.02	131.9±3.2	3.244±0.176	40.6±2.7	40.6±2.6	10/10	1.02±0.02	147.1±13.2	3.808±0.207	38.6±4.1	41.6±4.5	41.0±4.1
BT1537	HCK1_3	7.75	19/19	1.02±0.01	185.2±2.2	3.217±0.171	57.6±3.6	54.5±2.7	10/10	1.00±0.03	172.3±11.3	3.797±0.204	45.4±3.8	48.9±4.2	45.3±3.5
BT1536	HCK1_2	8.50	19/19	1.03±0.02	205.8±2.8	3.435±0.187	59.9±3.8	56.7±2.5	10/10	1.01±0.03	169.8±11.1	4.057±0.221	41.9±3.6	45.1±4.0	47.2±3.3
BT1535	HCK1_1	9.35	17/17	1.05±0.02	175.2±2.1	3.315±0.179	52.8±3.3	58.1±2.5	8/10	1.00±0.03	178.4±17.1	3.920±0.213	45.5±5.0	49.1±5.6	50.5±4.7
BT1534	Zill_3	1.30	24/24	1.03±0.03	52.6±0.5	3.515±0.204	15.0±1.0	–	–	–	–	–	–	–	–
BT1533	Zill_1	2.40	22/22	1.03±0.03	51.4±0.4	3.519±0.195	14.6±0.9	–	–	–	–	–	–	–	–

[1]Accepted in relation to measured number of aliquots.
[2]D_e uncertainties include a systematic error of 3% associated with β-source calibration. For IRSL, the residual dose remaining after 3 h exposure to a solar simulator was subtracted from the D_e values.

~20 and ~27 ka are condensed in time with the new model to a time window at ~26–24 ka (Fig. 9B). Finally, loading 3 (Fig. 9C) represents grain sizes >55 µm and most closely resembles the mean grain-size data set shown in Fig. 8 and described earlier. The sediment–age relationship of the grain-size data plotted with thin lines in Figs 8 and 9 is based on extrapolation beyond the youngest and oldest available luminescence ages and must therefore be interpreted with care.

Discussion

Luminescence methodology

Contrasting the new OSL against the IRSL data set generated on identical samples, it appears that in the upper part of the profile (<6 m) IRSL ages are systematically underestimated by ~1–5 ka as compared to OSL ages, although four out of the five samples in this section (BT1538–BT1543) overlap within 1σ uncertainty. If this observation is related to fading that was not adequately corrected for, remains open at this point. Slight inaccuracies in the chosen dose rate parameters (e.g. *a*-value) could likewise cause an offset between OSL and IRSL ages.

A somewhat different picture emerges for the lower part of the profile (>6 m), encompassing samples BT1535–BT1537. Here, two out of the three samples yield OSL and IRSL ages significantly different from each other (at 1σ), while IRSL ages underestimate OSL ages by ~4–15 ka. Both OSL and IRSL ages do not significantly increase with depth here, which could be explained either by high sedimentation rates at the base and below the soil complex of units V.I and V.II or by onset of dose saturation for both OSL and IRSL signals. Although OSL D_e values are well below the $2D_0$ threshold, the commonly accepted criterion for reliable SAR dose estimation, age underestimation of OSL fine grain samples cannot be ruled out. Such behaviour has frequently been reported from loess records and other environments across Eurasia (e.g. Lai 2010; Lowick & Preusser 2011; Kreutzer *et al.* 2012b; Moska *et al.* 2015, 2019) and associated with the differing shape of natural and laboratory-generated dose-response curves (Chapot *et al.* 2012; Timar-Gabor & Wintle 2013; Timar-Gabor *et al.* 2015). Consequently, these OSL ages could be regarded as minimum ages. Additionally, for reliable estimation of D_0, dose-response curves should be constructed up to full saturation (Timar-Gabor & Wintle 2013). For IRSL data, signal saturation is not considered a major problem with D_0 in the range 300–350 Gy.

Comparison with the previous IRSL chronology

The new OSL and IRSL chronologies of the upper part (<5 m) of the Hecklingen profile conform within uncertainties with the re-calculated IRSL ages by Krauß *et al.*
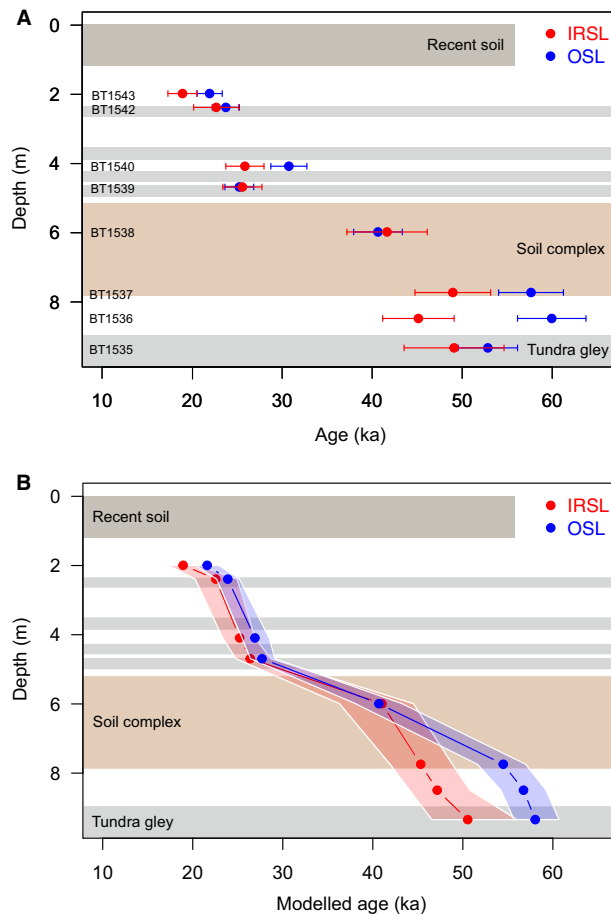
Fig. 4. A. Plot of the new OSL and IRSL ages of the Hecklingen site against stratigraphical information. All grey bars indicate weak tundra gley palaeosols, error bars represent 1σ uncertainty levels. B. Modelled new OSL and IRSL ages against stratigraphical information. The shaded polygons stand for 1σ uncertainty levels. It should be noted that the uncertainty of age information based on interpolation between calculated luminescence ages is larger than indicated in the plot.

(2016) (Tables 1, 5), with the new ages generally appearing to be slightly older. However, since the sampling positions of the two sets of samples (Fig. 5) are not identical, a direct numerical comparison including significance tests is not possible. In the lower part of the profile, the upper IRSL ages (BT1536 and C-L1309; unit VI.I) assigned to MIS 4 appear to be underestimated, while the lowermost IRSL age by Krauß *et al.* (2016) roughly corresponds to stratigraphical expectations. The OSL age of sample BT1535 (52.8±3.3 ka; unit VI.II) might be underestimated, as indicated by the DRT results of an adjacent sample (Table 3). A systematic underestimation of the Krauß *et al.* (2016) IRSL data cannot be confirmed, because some of the ages seem plausible with regard to the new OSL chronology (e.g. C-L1310) or show even an older age (C-L1308).

Comparing the dose rate data from Reinecke (2006) and Krauß *et al.* (2016) to those of the new OSL and

IRSL results, it becomes clear that determined radioelement concentrations and thus the total dose rate for the more recently taken samples are systematically higher, especially for the Hecklingen profile. In particular, the K and U values measured by α-counting and ICP-OES significantly exceed those determined by γ-ray spectrometry (K by ~16% and U by ~50%). Therefore, dose rates calculated for the new IRSL samples are on average ~25% greater than those of the previous samples. Despite intercalated zones of pedogenesis potentially enriched in radioactivity, loess is an overall homogeneous sediment, and within analytical uncertainties we could not establish a correlation between the presence of a palaeosol (tundra gley or the MIS 3 soil complex) at a sampling spot and the measured radioelement concentration. Since some of the samples were taken in approximately comparable stratigraphical positions, a systematic difference of the dose rate values of both data sets is hence unexpected and points to inaccuracies in some of the analytical procedures for dose rate determination. Consequently, some of the mismatch between old and new luminescence chronologies could be attributed to issues in dose rate assessment.

OSL ages of samples BT1536 (59.9±3.8 ka) and BT1537 (57.6±3.6 ka) support the previous assumption (Krauß *et al.* 2016) that the truncated transition zone of a former MIS 3 soil (unit V.II) and the loess layer below (unit VI.I) have a similar age and therefore the former soil must have developed in the loess layer. Furthermore, the age of sample BT1538 (40.6±2.7 ka) suggests indeed that the MIS 3 soil material (unit V.I) was re-located and pedogenically overprinted after re-deposition as previously proposed.

The new OSL ages at Zilly of ~15 ka are indistinguishable (within 1σ uncertainty) from the previous IRSL ages, irrespective of the sampling position. This seems to rule out substantial anomalous fading in the latter ages, being consistent with the observation that the newly generated IRSL ages show significant age underestimation only beyond 40 ka.

Identical OSL ages of samples BT1534 and BT1533 support the results of geochemical and grain-size proxies discussed in Krauß *et al.* (2016), indicating high accumulation rates of predominantly silt-sized (~80%), unaltered material during MIS 2.

Bayesian age-depth modelling

Generally, Bayesian age-depth models use the initial age information together with the stratigraphical principle of superposition commonly leading to a better understanding of the true age and reduced uncertainty (Bronk Ramsey 2009; Zeeden *et al.* 2018). Outliers can be problematic for such modelling approaches and affect ages and credible intervals for the entire modelled sequence. Some methods allow the setting of outlier
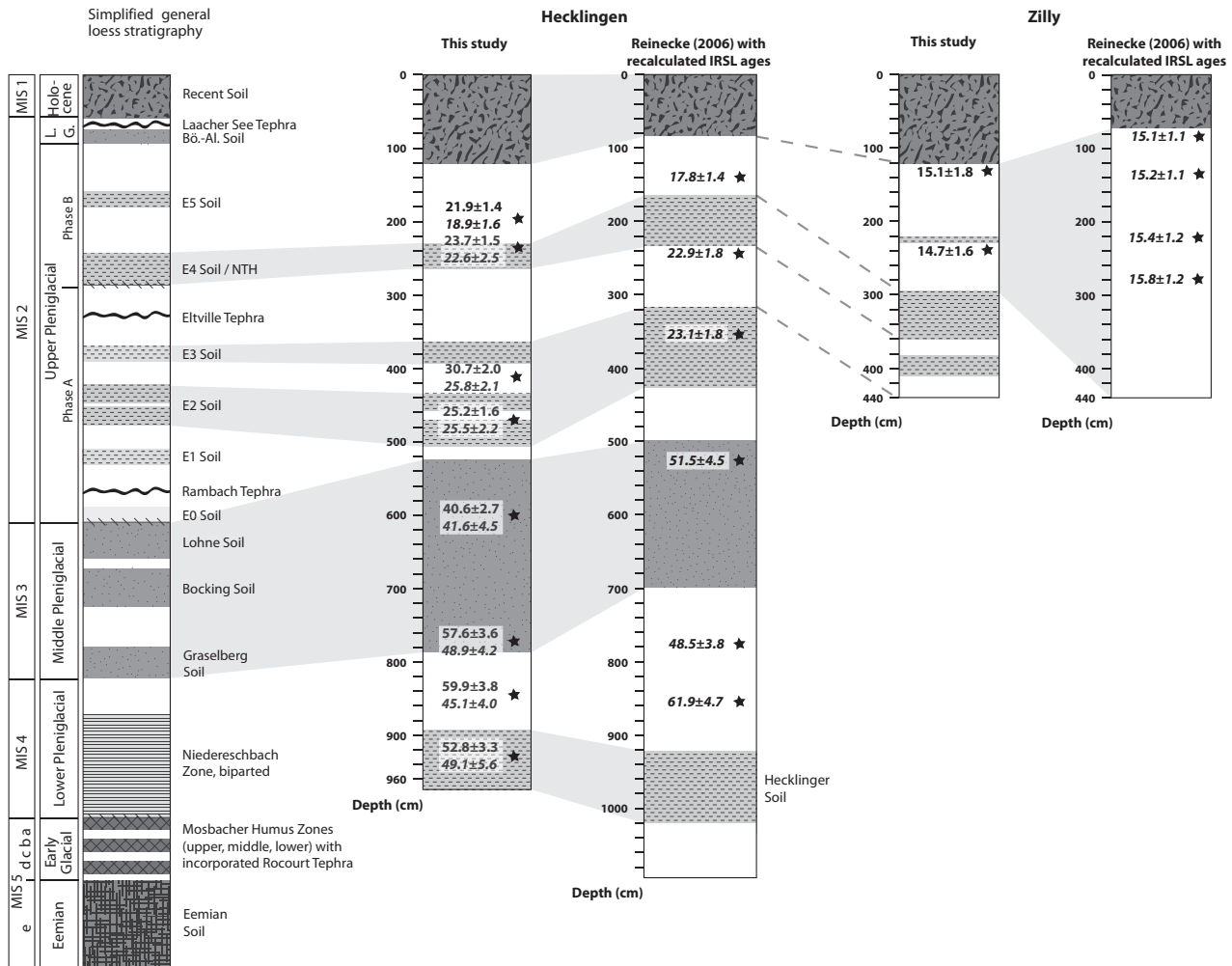
Fig. 5. Generalized LPS stratigraphy of central Europe after Zens *et al.* (2017; modified after Schönhals *et al.* 1964 and Bibus 2002) along with the stratigraphy and chronology of the Hecklingen and Zilly sites investigated in Krauß *et al.* (2016) and this study. OSL ages are shown together with IRSL ages (displayed in italics).

probabilities (Parnell 2018), which we did not include here.

The 1σ credible interval assumes that all ages are true (and no outliers) and that the uncertainty derived from luminescence dating is correct. Most models assume uncertainty to be fully random, which allows a maximum in uncertainty reduction. The ADMin model applied here (Zeeden *et al.* 2018) assumes the reported uncertainty to be correct, but deliberately does not make an initial assumption about which proportions of the reported uncertainty are systematic or random. Rather it derives this information from the data set itself in a probabilistic manner. This is expected to lead to less increase in accuracy, which, however, is more realistic for luminescence ages. Yet, an unsolved issue is the treatment of data points that might be subject to a systematic uncertainty larger than those for the remaining data points, or which are characterized by an asymmetric systematic uncertainty. For instance, this becomes relevant for luminescence ages probably underestimated as

indicated by diagnostic laboratory tests, or for luminescence ages derived from poorly bleached sediment such as soil that has undergone gelifluction. For those cases, a statistically valid procedure is still pending, but beyond the scope of this contribution.

For the Hecklingen profile, the modelled ages (both OSL and IRSL) show a consistent stratigraphy with increasing age corresponding to increasing depth. For most samples, original and modelled ages show overlapping 1σ uncertainty, and several samples hardly change in age. The modelled uppermost and lowermost samples are not obviously younger or older than expected, which is a good model outcome, as outermost samples can indicate modelling problems (Bronk Ramsey 2000; Steier & Rom 2000). In our data set, the age-depth modelling reduces 1σ uncertainty by 19 and 12% on average for OSL and IRSL ages, respectively, ranging from 1 to 37% and from −3 to 18% for individual samples. This corresponds to results by Zeeden *et al.* (2018), who found uncertainty reduction of 21–30% for a loess data
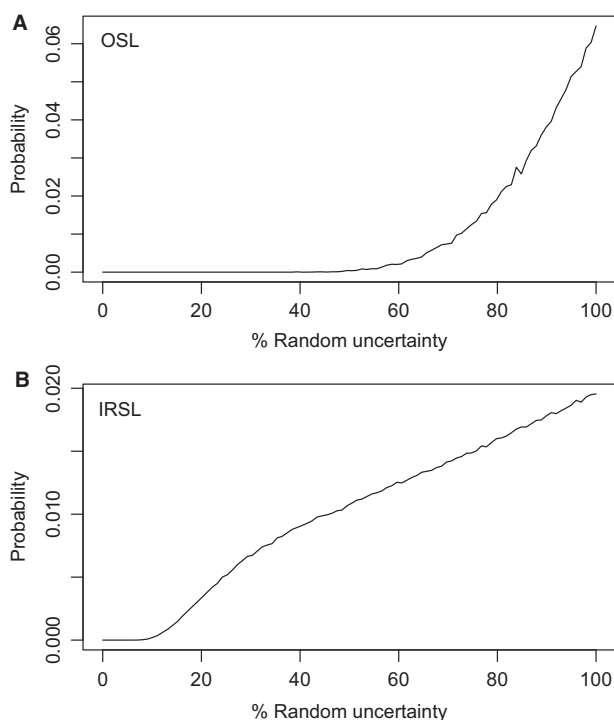
Fig. 6. Modelling results for the random and systematic uncertainty parts of the new OSL (A) and IRSL (B) ages from the Hecklingen profile. The graphs show probability density functions (PDFs) for the random uncertainty part inherent in both data sets, as derived from the approach by Zeeden *et al.* (2018).

set with more samples. The youngest IRSL sample showed an increase in uncertainty following age-depth modelling, which might be an issue of boundary effects in the modelling process.

Finally, it is possible that the age inversions in the OSL and IRSL data sets are not of pure statistical origin but related to geomorphic processes. The location of the two LPS close to the former ice margin favours periglacial processes such as gelifluction, leading to spatio-temporal variations in bleaching conditions and therefore potentially to age inversions. Likewise, temporal changes in dose rate induced by varying moisture/ice content in the sediment or secular disequilibria in the U decay series could also produce reversed ages (Degering & Degering 2020). The change in grain-size composition with a higher proportion of loading 1 at <4.70 m might indicate a shift in source area with material of different luminescence properties, hence potentially triggering age inversions as well.

Age-depth modelling and grain-size unmixing for an improved interpretation of palaeoenvironmental proxy data

The end member modelling results (Fig. 7) demonstrate how complex LPS are in their function of documenting palaeoenvironmental developments over time. The

loadings alone (Fig. 7A, B) would not allow a detailed evaluation of the proxy data since they represent the entire profile without distinguishing between different phases. This is especially problematic when LPS include different phases of soil development. Contextual knowledge about the investigated systems is therefore vital to interpret the results correctly (Dietze & Dietze 2019). Thus, the interpretation of the sequences attempted here additionally takes into account the results of Krauß *et al.* (2016).

In Hecklingen, loading 1 (Fig. 7A) very likely includes postdepositional soil formation and aeolian deposition of finer fractions without distinguishing between the two with depth (Fig. 7C). Vandenberghe *et al.* (2018) state that clay minerals might reach similar grain sizes in their pristine shape as dust sediments and hence recommend including all available site information (cf. Vandenberghe 2013; Schulte & Lehmkuhl 2018). Loading 3 (Fig. 7A) seems to include portions of aeolian but also slope wash deposits of coarser material. However, loading 2 (Fig. 7A) shows a single peak at 35 μm, lying within the range of European loess. Vandenberghe *et al.* (2018) and Dietze & Dietze (2019) suggest that it is possible to unmix grain-size composition and identify the primary windblown signal after alteration and potentially filter out the characteristic imprint of reworking processes. Thus, we interpret loading 2 as the primary loess end member representing dominant westerly wind directions (e.g. Renssen *et al.* 2007), since the two other loadings might display different geomorphic and pedogenic processes. The bottom of the sequence is mainly composed of loadings 1 and 2 (Fig. 7C). Following the penultimate argumentation, results display a phase of pronounced deposition of aeolian material at the bottom, which decreases continuously towards the top in favour of finer material, indicating successive soil development in the deposited loess material. The mean grain size combined with the Bayesian OSL age-depth model (Fig. 8) shows a substantial improvement in reasonable timing of the loess accumulation phase and first pedogenesis during MIS 3. Figure 9 gives a more detailed picture of the continuously lowering contribution of loading 2 towards pedogenesis, matching the timing of MIS 3 interstadials and soil development well.

Between 7 and 6.5 m depth, a sudden switch in the contribution of different loadings indicates an erosional event that might have truncated the assumed soil (Fig. 7C). Up to ~5 m depth loadings 1 and 3 contribute alternating but similar scores. This suggests shallow slope wash and re-deposition of soil sediment but also pedogenic overprinting by formation of finer grained secondary clay minerals. During weathering processes, iron oxides are released and material is coloured brownish to reddish (brunification), the primary minerals are transformed, and secondary clay minerals form as well
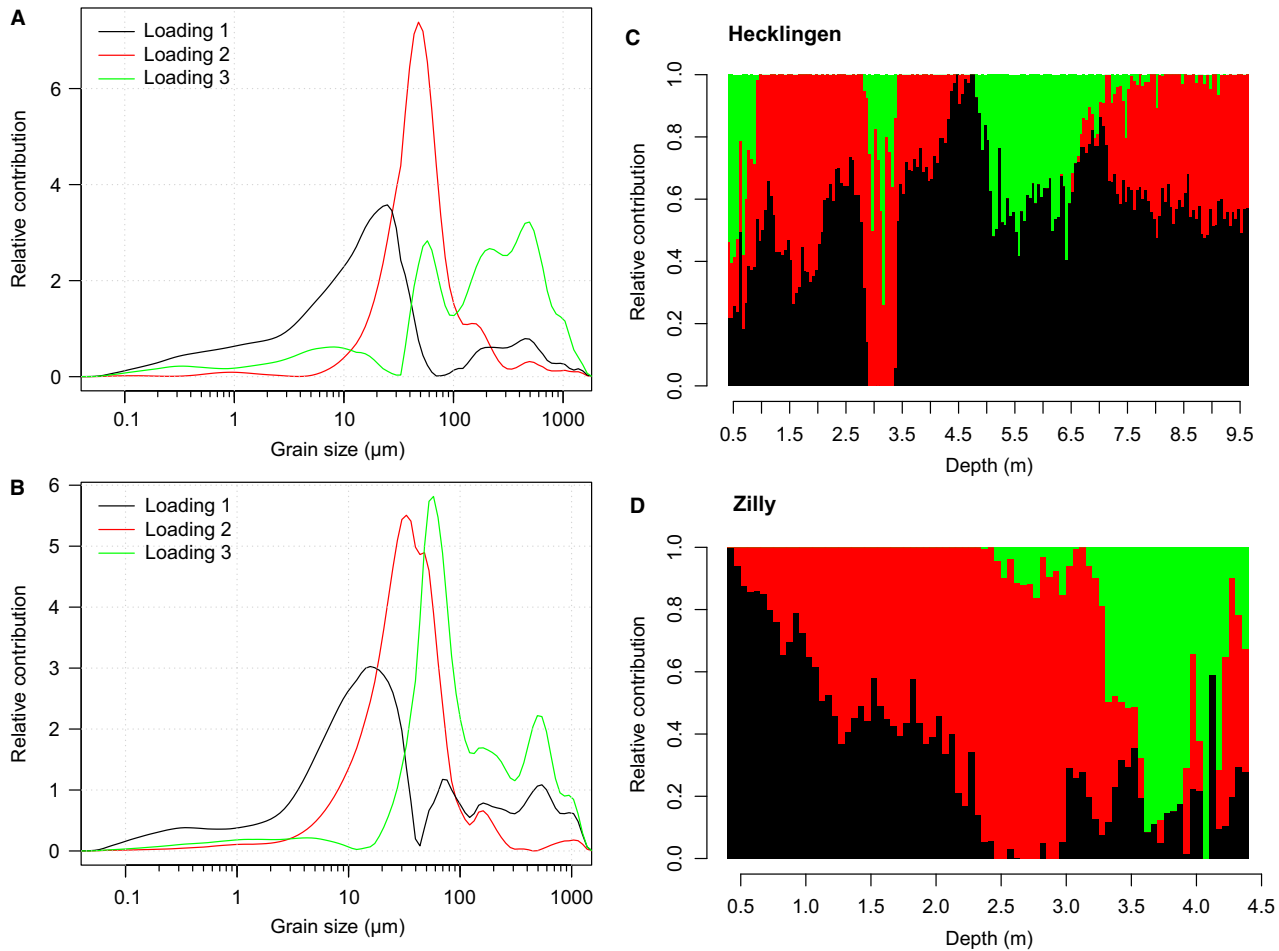
Fig. 7. End member loadings for the Hecklingen (A) and Zilly (B) profiles, as resulting from the EMMAgeo algorithm (Dietze *et al.* 2012; Dietze & Dietze 2016, 2019). The relative contribution of these loadings ('scores') vs. profile depth is shown in (C) and (D); the colours correspond to those used to depict the loadings in (A) and (B).

(loamification, e.g. Blume *et al.* 2016). Geochemical and colour data in Krauß *et al.* (2016) support the assumption of pedogenically overprinted soil sediment.

This phase is bordered by a 100% contribution of loading 1 at ~4.7 m, indicating either erosion followed by sedimentation or a rapid burial of the soil complex. Since no intact A-horizon was left and almost all palaeosols are more or less truncated, we propose the EMMA results to reflect erosion followed by loess accumulation. This agrees with the Bayesian OSL age model putting the end of the MIS 3 soil complex at ~29 ka (Figs 8, 9). The varying proportions between loadings 1 and 2 at ~4.5–3.5 m might represent tundra gleys (E0, E1, E2, Fig. 5).

At ~3.5 m loadings 2 and 3 solely make up the grain-size composition (Fig. 7C). Considering that loading 1 is completely missing, loading 3 might in this case represent rather aeolian deposition of coarser material than reworking of material. Further, the uniqueness of the layer (~3.4–2.8 m) also argues for a change of source contribution and therefore wind direction. Geochemical and colour data of Krauß *et al.* (2016) support this

assumption and indicate a shift of wind direction towards stronger and more frequent easterly winds during a postulated time frame confined more or less to the LGM. The strong influence of the SIS and its last maximum extent should receive more attention as a major cause for these shifts than the overall influence of the Greenland Ice Sheet. The timing and the number of ice advances of the SIS are still a matter of debate and under investigation (Lüthgens *et al.* 2020).

The Bayesian OSL age model puts this accumulation phase in a narrower time window of 26–24 ka as compared to the linear IRSL age model (Figs 8, 9). Considering the findings of Hughes *et al.* (2016) and Lüthgens & Böse (2011), it is thus possible that this accumulation phase in MIS 2 is connected to the most southerly extent of the SIS and its stronger influence on atmospheric circulations in the region, causing easterly winds with strong dust storms. However, the most pronounced east wind activity in the Eifel (western Germany) appears to fall into the period 23–20 ka with a short interruption near 21 ka (Römer *et al.* 2016).
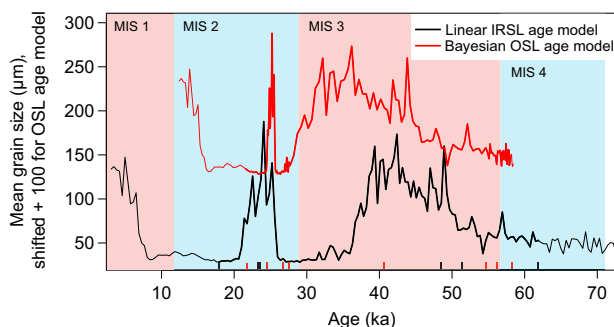
Fig. 8. Hecklingen mean grain-size data (Krauß *et al.* 2016, 2017) on the original age scale (black lines) based on the 'old' set of IRSL ages and on the Bayesian OSL age model (red lines). Thin lines indicate linear extrapolation of ages beyond outer ages and should be considered with caution. The rugs on the inward side of the *x*-axis symbolize the individual ages considered for age-depth modelling. Boundaries of indicated Marine Isotope Stages (MIS) are taken from https://www. lorraine-lisiecki.com/LR04_MISboundaries.txt (16th April 2020), except for the MIS 1/2 boundary, which is based on Rasmussen *et al.* (2006).

Hughes *et al.* (2016) showed that the end of this period accords with the Pomeranian ice limit across northern Germany and Poland.

Further up-profile, the dominance of loading 1 suggests a further tundra gley (E4; Fig. 5) at 2.8–2 m. Between 2 and 1.2 m the slight dominance of loading 2 indicates the last enhanced accumulation of aeolian material. Above, a 1.2-m-thick Holocene soil developed, showing reworking of material probably due to deep ploughing during the 40 years of the German Democratic Republic.

As the time frame preserved is different at Zilly (Fig. 5), loadings show a different composition than at Hecklingen (Fig. 7A, C). However, loading 2 could be interpreted as the primary loess end member displaying regular westerly wind induced dust storms. Loadings 1 and 3 also seem to include aeolian components but might as well show a mixture of process signals (Fig. 7B). At the bottom of the sequence, EMMA suggests a different input source through high relative contributions by loading 3 (Fig. 7D), indicating a shift towards a coarser aeolian component. However, at Hecklingen the scores of loadings 2 and 3 behave similarly during the most southerly extent of the SIS, while they behave contrarily at the bottom of the Zilly profile (Fig. 7D). This suggests that at Zilly a short phase during the deposition of the last cover loess and post-LGM ice sheet retreat initiated a switch of source material assuming that loading 2 represents dominantly westerly winds. At ~3–2.5 m the sediment composition is almost solely explained by loading 2; loading 1 takes the lead from ~1.2 m towards the top. Above 2.2 m, loading 2 represents a phase of windblown sediments, in which the Holocene soil successively developed. As loading 3 is missing for depths <1 m, the modern soil was not ploughed deeply, unlike in Hecklingen.

Comparison with neighbouring loess areas

The following comparison of our results from the northern Harz foreland with those from neighbouring loess areas is restricted to well-studied LPS southeast and east of our study area. Further to the west or southwest well-studied LPS appear only quite far away along the Lower Rhine Embayment with different actual climate and much greater distance from the LGM ice advance (see Fig. 1). Thick loess occurrences in Saxony and Lower Silesia (western Poland), however, are also situated at the periphery of the Central European Lowland towards the Upland (Ore Mountains, Sudetes) and affected by the drier and more continental climate in the rain-shadow of the Harz Mountains and the northern ridges of the Bohemian Massif.

The 'Gleinaer Bodenkomplex' (Gleina Pedocomplex) was supposed to represent cumulative interstadial pedogenesis from the upper part of the Middle Weichselian (Lieberoth 1963). More recent studies (Meszner *et al.* 2013, 2014) on Saxonian LPS and a composite profile demonstrated, however, that based on OSL dating this complex marks an important gap in loess sedimentation between 60 and 30 ka in central Europe. Therefore, this sequence is designated as the 'Gleina Complex' (without the word 'Boden', i.e. 'soil'). As far as loess-like material of the Gleina Complex (III) is preserved at all, it consists of brownish and gleyic remnants of interstadial soils and is characterized by repeated re-deposition. The Gleina Complex is estimated to be some 30 ka old, following a phase with strong erosion. The thick loess above the Gleina Complex (~30–18 ka) looks foliated in its lower part (IIb) and like homogenous loess in its upper part (IIa). So far, a strong similarity between loess of the Harz foreland and of Saxony is apparent.

The composite profile of Saxonian LPS reaches further back in time than the Hecklingen profile, and a comparison of both below the Gleina Complex is questionable with respect to the present database. The drier position of Hecklingen compared to Gleina may explain the preservation of the Hecklingen soil complex despite some evidence of re-deposition (coarser embedded material, loading 3 in Figs 7C, 9C).

Meszner *et al.* (2014) pointed out two major phases with loess accumulation throughout the northern branch of the European loess belt. This can be confirmed from Hecklingen via Saxony to Silesia, where a ~3-m-thick interstadial soil complex is preserved between ~2 m of underlying and ~6 m overlying stadial loess at the Lower Silesian LPS Biały Kościół, 40 km south of Wrocław (Jary & Ciszek 2013; Moska *et al.* 2019). According to luminescence ages, a hiatus accompanies the interstadial soil complex, which may be some 15 to 27 ka long (Moska *et al.* 2019). In the section at Zaprężyn, 16 km northeast of Wrocław and closer to the LGM
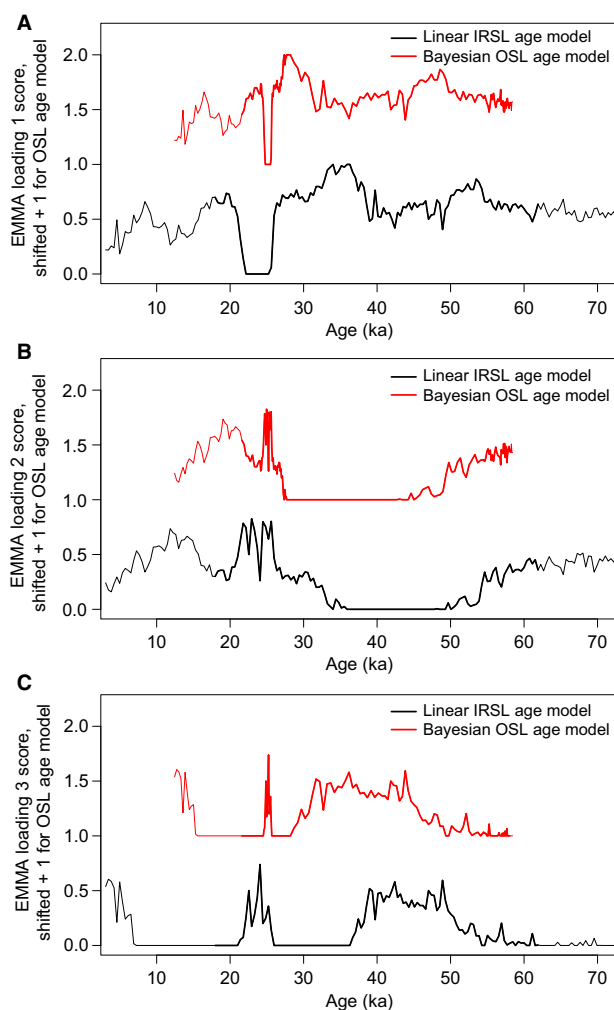
Fig. 9. Hecklingen scores (relative contribution) of the three end member loadings (A, B, C) derived from application of the EMMAgeo algorithm (Dietze *et al.* 2012; Dietze & Dietze 2016, 2019), plotted against the 'old' IRSL model (black lines) and the new Bayesian OSL model (red lines).

ice advance, this erosional unconformity is twofold and ~34 ka long.

Conclusions

We established new OSL and IRSL chronologies for two LPS (Hecklingen, Zilly) in the northern Harz foreland, which are of particular interest for palaeoenvironmental research due to their proximity to the maximum extent of the SIS. Application of a Bayesian age-depth model was successful in resolving age inversions in the Hecklingen OSL and IRSL records and produced a consistent age-depth relationship. Thereby, we significantly increased precision of individual ages (by ~19 and ~12% on average for OSL and IRSL). Although fading-corrected, IRSL underestimates OSL in the lower part of the Hecklingen

profile, and further inferences were based on the OSL data set. While the modelled age-depth relationship technically facilitates the calculation of sedimentation rates, its validity has to be carefully assessed owing to the non-continuous nature of the LPS at Hecklingen, featuring erosive phases and re-location through slope wash.

The effect of the new Bayesian OSL age model for the Hecklingen site as compared to previous IRSL ages was demonstrated with the grain-size data set compiled in a precursor study (Krauß *et al.* 2016): input of coarse aeolian material extends over a much longer period in MIS 3 until its termination at ~29 ka and the sharp peak of mean grain size in MIS 2 can be constrained to a much shorter interval (~26–24 ka). This distinct accumulation of relatively coarse aeolian sediments in MIS 2 can thus be more confidently correlated to the maximum extent of the SIS and strong easterly winds prevailing during that period.

Finally, EMMA of the grain-size data by Krauß *et al.* (2016) allowed us to identify three fundamental end members for the Hecklingen and Zilly sections that can be interpreted to represent characteristic geomorphic processes such as the deposition of primary loess, slope wash of relatively coarse material or the breakdown of grain sizes due to pedogenesis. Combining the EMMA results with the new Bayesian OSL age model created a high-resolution record of environmental dynamics tracing changes in dominating geomorphic processes independent of imposed grain-size classifications.

We conclude that the new chronometric data along with the Bayesian age-depth and grain-size end member modelling offered a series of new insights into palaeoenvironmental dynamics in the study area. As such, these modelling approaches might represent an incentive to re-evaluate existing LPS or other sedimentary data sets to fully unfold the potential of these records.

Author contributions. – LK, CZ and FL carried out fieldwork and took the samples. CS was responsible for luminescence dating and related analyses. CZ, LK and CS did the Bayesian age-depth modelling, EMMA and the interpretation of results. FL, LK and CZ prepared part of the figures. LZ and FL helped to discuss the data and to edit the manuscript. CS wrote the manuscript and prepared part of the figures with significant input from all co-authors.

References

Aitken, M. 1985: *Thermoluminescence Dating*. 359 pp. Academic Press, London.

Assallay, A. M., Rogers, C. D. F., Smalley, I. J. & Jefferson, I. F. 1998: Silt: 2–62 μm, 9–4φ. *Earth-Science Reviews 45*, 61–88.

Atterberg, A. 1905: Die rationelle Klassifikation der Sande und Kiese. *Chemiker-Zeitung 29*, 195–198.

Balescu, S., Lamothe, M., Mercier, N., Huot, S., Balteanu, D., Billard, A. & Hus, J. 2003: Luminescence chronology of Pleistocene loess deposits from Romania: testing methods of age correction for anomalous fading in alkali feldspars. *Quaternary Science Reviews 22*, 967–973.

Berger, G. W., Mulhern, P. J. & Huntley, D. J. 1980: Isolation of silt-sized quartz from sediments. *Ancient TL 11*, 8–9.

Bibus, E. 2002: Zum Quartär im mittleren Neckarraum: Reliefentwicklung, Löß/Paläobodensequenzen, Paläoklima. *Tübinger Geographische Arbeiten D8.*, 235 pp.

Blott, S. J. & Pye, K. 2012: Particle size scales and classification of sediment types based on particle size distributions: review and recommended procedures. *Sedimentology 59*, 2071–2096.

Blume, H.-P., Brümmer, G. W., Fleige, H., Horn, R., Kandeler, E., Kögel-Knabner, I., Kretzschmar, R., Stahr, K. & Wilke, B.-M. 2016: *Scheffer/Schachtschabel - Soil Science*. 636 pp. Springer, Heidelberg.

Brennan, B. J., Lyons, R. G. & Phillips, S. W. 1991: Attenuation of alpha particle track dose for spherical grains. *Nuclear Tracks and Radiation Measurements 18*, 249–253.

Bronk Ramsey, C. 1995: Radiocarbon calibration and analysis of stratigraphy: the OxCal program. *Radiocarbon 37*, 425–430.

Bronk Ramsey, C. 2000: Comment on 'The use of Bayesian Statistics for [14]C Dates of Chronologically ordered samples: A Critical Analysis'. *Radiocarbon 42*, 199–202.

Bronk Ramsey, C. 2009: Bayesian analysis of radiocarbon dates. *Radiocarbon 51*, 337–360.

Brosche, K.-U. & Walther, M. 1978: Die jungpleistozänen Deckschichten der Braunkohletagebaue der Braunschweigischen Kohlebergwerke (BKB) zwischen Helmstedt und Schöningen. *E&G Quaternary Science Journal 28*, 51–67.

Buck, C. E., Cavanagh, G. & Litton, C. 1996: *Bayesian Approach to Interpreting Archaeological Data*. 402 pp. Wiley, Chichester.

Buck, C. E., Kenworthy, J. B., Litton, C. D. & Smith, A. F. M. 1991: Combining archaeological and radiocarbon information: a Bayesian approach to calibration. *Antiquity 65*, 808–821.

Chapot, M. S., Roberts, H. M., Duller, G. A. T. & Lai, Z. P. 2012: A comparison of natural- and laboratory-generated dose response curves for quartz optically stimulated luminescence signals from Chinese Loess. *Radiation Measurements 47*, 1045–1052.

Clark, P. U., Dyke, A. S., Shakun, J. D., Carlson, A. E., Clark, J., Wohlfarth, B., Mitrovica, J. X., Hostetler, S. W. & McCabe, A. M. 2009: The Last Glacial Maximum. *Science 325*, 710–714.

Combès, B. & Philippe, A. 2017: Bayesian analysis of individual and systematic multiplicative errors for estimating ages with stratigraphic constraints in optically stimulated luminescence dating. *Quaternary Geochronology 39*, 24–34.

Degering, D. & Degering, A. 2020: Change is the only constant - time-dependent dose rates in luminescence dating. *Quaternary Geochronology 58*, 101074, https://doi.org/10.1016/j.quageo.2020.101074.

Dietze, E. & Dietze, M. 2019: Grain-size distribution unmixing using the R package EMMAgeo. *E&G Quaternary Science Journal 68*, 29–46.

Dietze, E., Hartmann, K., Diekmann, B., IJmker, J., Lehmkuhl, F., Opitz, S., Stauch, G., Wünnemann, B. & Borchers, A. 2012: An end-member algorithm for deciphering modern detrital processes from lake sediments of Lake Donggi Cona, NE Tibetan Plateau, China. *Sedimentary Geology 243–244*, 169–180.

Dietze, M. & Dietze, E. 2016: EMMAgeo: End-member Modelling of Grain-Size Data. https://cran.r-project.org/web/packages/EMMAgeo/

Dobrzański, B., Kowaliński, S., Kuznicki, F., Witek, T. & Zawadzki, S. 1974: *Soil Map of Poland*, Polska Akademia Nauk, Warsaw.

Doeglas, D. J. 1968: Grain-size indices, classification and environment. *Sedimentology 10*, 83–100.

Döring, J. 2004: Zu den Klimaverhältnissen im östlichen Harzvorland. *Hercynia N.F. 37*, 137–154.

Duller, G. A. T. 2015: The Analyst software package for luminescence data: overview and recent improvements. *Ancient TL 33*, 35–42.

Durcan, J. A., King, G. E. & Duller, G. A. T. 2015: DRAC: dose rate and age calculator for trapped charge dating. *Quaternary Geochronology 28*, 54–61.

Ehlers, J., Grube, A., Stephan, H. J. & Wansa, S. 2011: Pleistocene glaciation of North Germany – New results. *In* Ehlers, J., Gibbard, P. L. & Hughes, P. D. (eds.): *Quaternary Glaciation – Extent and Chronology. A Closer Look*, 149–162. Developments in Quaternary Science 15.

Fabig, I. 2007: *Die Niederschlags- und Starkregenentwicklung der letzten 100 Jahre im Mitteldeutschen Trockengebiet als Indikatoren möglicher Klimaänderungen*. Ph.D. thesis, Martin-Luther-University Halle-Wittenberg, 186 pp.

Faust, D., Yanes, Y., Willkommen, T., Roettig, C. B., Richter, D., Suchodoletz, H. & Zöller, L. 2015: A contribution to the understanding of late Pleistocene dune sand-paleosol-sequences in Fuerteventura (Canary Islands). *Geomorphology 246*, 290–304.

Fenn, K., Durcan, J. A., Thomas, D. S. G. & Banak, A. 2020: A 180 ka record of environmental change at Erdut (Croatia): a new chronology for the loess–palaeosol sequence and its implications for environmental interpretation. *Journal of Quaternary Science 35*, 582–593.

Frechen, M. & Schirmer, W. 2011: Luminescence chronology of the Schwalbenberg II Loess in the Middle Rhein Valley. *E&G Quaternary Science Journal 60*, 78–89.

Galbraith, R., Roberts, R., Laslett, G., Yoshida, H. & Olley, J. 1999: Optical dating of single and multiple grains of quartz from Jinmium rock shelter, northern Australia: part I, experimental design and statistical models. *Archaeometry 42*, 339–364.

Gan, S. Q. & Scholz, C. A. 2017: Skew normal distribution deconvolution of grain-size distribution and its application to 530 samples from Lake Bosumtwi, Ghana. *Journal of Sedimentary Research 87*, 1214–1225.

Gehrt, E. 1994: *Die äolischen Sedimente im Bereich der nördlichen Lössgrenze zwischen Leine und Oker und deren Einflüsse auf die Bodenentwicklung*. Ph.D. thesis, Göttingen University, 217 pp.

Gehrt, E. & Hagedorn, J. 1996: Zur Entstehung der nördlichen Lössgrenze in Mitteleuropa. Landesamt für Natur und Umwelt Schleswig-Holstein, Abteilung Geologie/Boden. Festschrift Prof. Dr. Stremme, 59–66.

Guérin, G., Mercier, N. & Adamiec, G. 2011: Dose-rate conversion factors: update. *Ancient TL 29*, 5–8.

Guérin, G., Mercier, N., Nathan, R., Adamiec, G. & Lefrais, Y. 2012: On the use of the infinite matrix assumption and associated concepts: a critical review. *Radiation Measurements 47*, 778–785.

Haase, G., Lieberoth, I. & Ruske, R. 1970: Sedimente und Paläoböden im Lößgebiet. *In* Richter, H., Haase, G., Lieberoth, I. & Ruske, R. (eds.): *Periglazial – Löß – Paläolithikum im Jungpleistozän der Deutschen Demokratischen Republik*, 99–212. Petermanns Geographische Mitteilungen 274.

Hilgers, A., Gehrt, E., Janotta, A. & Radtke, U. 2001: A contribution to the dating of the northern boundary of the Weichselian Loess Belt in Northern Germany by luminescence dating and pedological analysis. *Quaternary International 76–77*, 191–200.

Hughes, A. L. C., Gyllencreutz, R., Lohne, Ø. S., Mangerud, J. & Svendsen, J. I. 2016: The last Eurasian ice sheets - a chronological database and time-slice reconstruction, DATED-1. *Boreas 45*, 1–45.

Huntley, D. J. & Lamothe, M. 2001: Ubiquity of anomalous fading in K-feldspars and the measurement and correction for it in optical dating. *Canadian Journal of Earth Sciences 38*, 1093–1106.

Jary, Z. & Ciszek, D. 2013: Late Pleistocene loess-palaeosol sequences in Poland and western Ukraine. *Quaternary International 296*, 37–50.

Karger, D. N., Conrad, O., Böhner, J., Kawohl, T., Kreft, H., Soria-Auza, R. W., Zimmermann, N. E., Linder, H. P. & Kessler, M. 2017: Climatologies at high resolution for the earth's land surface areas. *Scientific Data 4*, 170122, https://doi.org/10.1038/sdata.2017.122.

Krauß, L., Schmidt, G., Zierdt, M. & Frühauf, M. 2013: Experimentelle Bestimmung präferenzieller Fließpfade infiltrierten Niederschlags

am Beispiel einer Schwarzerde und einer Pararendzina der Querfurter Platte. *Hercynia N.F. 46*, 21–40.

Krauß, L., Zens, J., Zeeden, C., Schulte, P., Eckmeier, E. & Lehmkuhl, F. 2016: A multi-proxy analysis of two loess-paleosol sequences in the Northern Harz Foreland, Germany. *Palaeogeography, Palaeoclimatology, Palaeoecology 461*, 401–417.

Krauß, L., Zens, J., Zeeden, C., Schulte, P., Eckmeier, E. & Lehmkuhl, F. 2017: Grain size analyses of loess-paleosol sequence Hecklingen. PANGAEA. https://doi.org/10.1016/j.palaeo.2016.09.001.

Kreutzer, S. 2020: calc_FadingCorr(): apply a fading correction according to Huntley & Lamothe (2001) for a given g-value and a given tc. Function version 0.4.2. *In* Kreutzer, S., Burow, C., Dietze, M., Fuchs, M.C., Schmidt, C., Fischer, M. & Friedrich, J. *Luminescence: Comprehensive Luminescence Dating Data Analysis. R package version 0.9.8.9000-69.* https://CRAN.R-project.org/package=Luminescence

Kreutzer, S., Fuchs, M., Meszner, S. & Faust, D. 2012b: OSL chronostratigraphy of a loess-palaeosol sequence in Saxony/Germany using quartz of different grain sizes. *Quaternary Geochronology 10*, 102–109.

Kreutzer, S., Schmidt, C., Fuchs, M. C., Dietze, M., Fischer, M. & Fuchs, M. 2012a: Introducing an R package for luminescence dating analysis. *Ancient TL 30*, 1–8.

Lai, Z. P. 2010: Chronology and the upper dating limit for loess samples from Luochuan section in the Chinese Loess Plateau using quartz OSL SAR protocol. *Journal of Asian Earth Sciences 37*, 176–185.

Lanos, P. & Dufresne, P. 2019: *ChronoModel version 2.0: Software for Chronological Modelling of Archaeological Data using Bayesian Statistics.* https://chronomodel.com

Lehmkuhl, F., Pötter, S., Pauligk, A. & Bösken, J. 2018: Loess and other quaternary sediments in Germany. *Journal of Maps 14*, 330–340.

Lehmkuhl, F., Zens, J., Krauß, L., Schulte, P. & Kels, H. 2016: Loess-paleosol sequences at the northern European loess belt in Germany: distribution, geomorphology and stratigraphy. *Quaternary Science Reviews 153*, 11–30.

Lieberoth, I. 1963: Lößsedimentation und Bodenbildung während des Pleistozäns in Sachsen. *Geologie 12*, 149–187.

Lowick, S. E. & Preusser, F. 2011: Investigating age underestimation in the high dose region of optically stimulated luminescence using fine grain quartz. *Quaternary Geochronology 6*, 33–41.

Lüthgens, C. & Böse, M. 2011: Chronology of Weichselian main ice marginal positions in north-eastern Germany. *E&G Quaternary Science Journal 60*, 236–247.

Lüthgens, C., Hardt, J. & Böse, M. 2020: Proposing a new conceptual model for the reconstruction of ice dynamics in the SW sector of the Scandinavian Ice Sheet (SIS) based on the reinterpretation of published data and new evidence from optically stimulated luminescence (OSL) dating. *E&G Quaternary Science Journal 69*, 201–223.

Mauz, B., Packman, S. & Lang, A. 2006: The alpha effectiveness in silt-sized quartz: new data obtained by single and multiple aliquot protocols. *Ancient TL 24*, 47–52.

Meszner, S., Kreutzer, S., Fuchs, M. & Faust, D. 2013: Late Pleistocene landscape dynamics in Saxony, Germany: paleoenvironmental reconstruction using loess-paleosol sequences. *Quaternary International 296*, 94–107.

Meszner, S., Kreutzer, S., Fuchs, M. & Faust, D. 2014: Identifying depositional and pedogenetic controls of Late Pleistocene loess-paleosol sequences (Saxony, Germany) by combined grain size and microscopic analyses. *Zeitschrift für Geomorphologie, Supplementary Issues 58*, 63–90.

Meyers, S. R. 2014: Astrochron: An R Package for Astrochronology. https://CRAN.R-project.org/package=astrochron

Millard, A. R. 2004: Taking Bayes beyond radiocarbon: Bayesian approaches to some other chronometric methods. *In* Buck, C. E. & Millard, A. R. (eds.): *Tools for Constructing Chronologies, Lecture Notes in Statistics*, 231–248. Springer, London.

Moska, P., Jary, Z., Adamiec, G. & Bluszcz, A. 2015: OSL chronostratigraphy of a loess-palaeosol sequence in Złota using quartz and polymineral fine grains. *Radiation Measurements 81*, 23–31.

Moska, P., Jary, Z., Adamiec, G. & Bluszcz, A. 2019: Chronostratigraphy of a loess-palaeosol sequence in Biały Kościół, Poland using OSL and radiocarbon dating. *Quaternary International 502*, 4–17.

Murray, A. S. & Wintle, A. G. 2000: Luminescence dating of quartz using an improved single-aliquot regenerative-dose protocol. *Radiation Measurements 32*, 57–73.

Murray, A. S. & Wintle, A. G. 2003: The single aliquot regenerative dose protocol: potential for improvements in reliability. *Radiation Measurements 37*, 377–381.

Noppradit, P., Symanczyk, A., Zöller, L., Brückner, H. & Stock, F. 2018: Methodological approach for dating harbor sediments by using luminescence dating—a case study in Ephesus, Western Turkey. *Archaeological and Anthropological Sciences 11*, 3143–3153.

Parnell, A. 2018: *Bchron: Radiocarbon Dating, Age-Depth Modelling, Relative Sea Level Rate Estimation, and Non-Parametric Phase Modelling.* https://CRAN.R-project.org/package=Bchron

Paterson, G. A. & Heslop, D. 2015: New methods for unmixing sediment grain size data. *Geochemistry, Geophysics, Geosystems 16*, 4494–4506.

Perić, Z., Adolphi, E. L., Stevens, T., Újvári, G., Zeeden, C., Buylaert, J.-P., Marković, S. B., Hambach, U., Fischer, P., Schmidt, C., Schulte, P., Huayu, L., Shuangwen, Y., Lehmkuhl, F., Obreht, I., Veres, D., Thiel, C., Frechen, M., Jain, M., Vött, A., Zöller, L. & Gavrilov, M. B. 2019: Quartz OSL dating of late quaternary Chinese and Serbian loess: a cross Eurasian comparison of dust mass accumulation rates. *Quaternary International 502*, 30–44.

Poser, H. 1951: Die nördliche Lößgrenze in Mitteleuropa und das spätglaziale Klima. *E&G Quaternary Science Journal 1*, 27–55.

Preusser, F. 2003: IRSL dating of K-rich feldspars using the SAR protocol: comparison with independent age control. *Ancient TL 21*, 17–23.

R Core Team 2020: *R: A language and environment for statistical computing.* Vienna, Austria: R Foundation for Statistical Computing. https://www.R-project.org/

Rasmussen, S. O., Andersen, K. K., Svensson, A. M., Steffensen, J. P., Vinther, B. M., Clausen, H. B., Siggaard-Andersen, M.-L., Johnsen, S. J., Larsen, L. B., Dahl-Jensen, D., Bigler, M., Röthlisberger, R., Fischer, H., Goto-Azuma, K., Hansson, M. E. & Ruth, U. 2006: A new Greenland ice core chronology for the last glacial termination. *Journal of Geophysical Research 111*, D6, https://doi.org/10.1029/2005JD006079.

Reinecke, V. 2006: Untersuchungen zur mittel- und jungpleistozänen Reliefentwicklung und Morphodynamik im nördlichen Harzvorland. *Aachener Geographische Arbeiten 43*, 170 pp.

Renssen, H., Kasse, C., Vandenberghe, J. & Lorenz, S. J. 2007: Weichselian Late Pleniglacial surface winds over northwest and central Europe: a model–data comparison. *Journal of Quaternary Science 22*, 281–293.

Rhodes, E. J., Bronk Ramsey, C., Outram, Z., Batt, C., Willis, L., Dockrill, S. & Bond, J. 2003: Bayesian methods applied to the interpretation of multiple OSL dates: high precision sediment ages from Old Scatness Broch excavations, Shetland Isles. *Quaternary Science Reviews 22*, 1231–1244.

Römer, W., Lehmkuhl, F. & Sirocko, F. 2016: Late Pleistocene aeolian dust provenances and wind direction changes reconstructed by heavy mineral analysis of the sediments of the Dehner dry maar (Eifel, Germany). *Global and Planetary Change 147*, 25–39.

Rother, H., Shulmeister, J. & Rieser, U. 2010: Stratigraphy, optical dating chronology (IRSL) and depositional model of pre-LGM glacial deposits in the Hope Valley, New Zealand. *Quaternary Science Reviews 29*, 576–592.

Schmidt, C., Bösken, J. & Kolb, T. 2018: Is there a common alpha-efficiency in polymineral samples measured by various infrared stimulated luminescence protocols? *Geochronometria 45*, 160–172.

Schmidt, E. D., Semmel, A. & Frechen, M. 2011: Luminescence dating of the loess/palaeosol sequence at the gravel quarry Gaul/Weilbach, Southern Hesse (Germany). *E&G Quaternary Science Journal 60*, 116–125.

Schönhals, E., Rohdenburg, H. & Semmel, A. 1964: Ergebnisse neuerer Untersuchungen zur Würmlöß-Gliederung in Hessen. *E&G Quaternary Science Journal 15*, 199–206.

Schulte, P. & Lehmkuhl, F. 2018: The difference of two laser diffraction patterns as an indicator for post-depositional grain size reduction in loess-paleosol sequences. *Palaeogeography, Palaeoclimatology, Palaeoecology 509*, 126–136.

Steier, P. & Rom, W. 2000: The use of Bayesian statistics for ^{14}C dates of chronologically ordered samples: a critical analysis. *Radiocarbon 42*, 183–198.

Timar-Gabor, A. & Wintle, A. G. 2013: On natural and laboratory generated dose response curves for quartz of different grain sizes from Romanian loess. *Quaternary Geochronology 18*, 34–40.

Timar-Gabor, A., Constantin, D., Buylaert, J. P., Jain, M., Murray, A. S. & Wintle, A. G. 2015: Fundamental investigations of natural and laboratory generated SAR dose response curves for quartz OSL in the high dose range. *Radiation Measurements 81*, 150–156.

Újvári, G., Kok, J. F., Varga, G. & Kovács, J. 2016: The physics of wind-blown loess: implications for grain size proxy interpretations in Quaternary paleoclimate studies. *Earth-Science Reviews 154*, 247–278.

Vandenberghe, J. 2013: Grain size of fine-grained windblown sediment: a powerful proxy for process identification. *Earth-Science Reviews 121*, 18–30.

Vandenberghe, J., Sun, Y., Wang, X., Abels, H. A. & Liu, X. 2018: Grain-size characterization of reworked fine-grained aeolian deposits. *Earth-Science Reviews 177*, 43–52.

Wallinga, J., Murray, A. S., Duller, G. A. T. & Törnqvist, T. E. 2001: Testing optically stimulated luminescence dating of sand-sized quartz and feldspar from fluvial deposits. *Earth and Planetary Science Letters 193*, 617–630.

Wallinga, J., Murray, A. S. & Wintle, A. G. 2000: The single-aliquot regenerative-dose (SAR) protocol applied to coarse-grain feldspar. *Radiation Measurements 32*, 529–533.

Wintle, A. G. 1973: Anomalous fading of thermoluminescence in mineral samples. *Nature 245*, 143–144.

Wintle, A. G. & Murray, A. S. 2006: A review of quartz optically stimulated luminescence characteristics and their relevance in single-aliquot regeneration dating protocols. *Radiation Measurements 41*, 369–391.

Zagwijn, W. H. & Van Staalduinen, C. J. (eds.) 1975: *Toelichtingen bij the geologische overzichtskarten van Nederland*. 134 pp. Rijks Geologische Dienst, Haarlem.

Zeeden, C., Dietze, M. & Kreutzer, S. 2018: Discriminating luminescence age uncertainty composition for a robust Bayesian modelling. *Quaternary Geochronology 43*, 30–39.

Zens, J., Zeeden, C., Römer, W., Fuchs, M., Klasen, N. & Lehmkuhl, F. 2017: The Eltville Tephra (Western Europe) age revised: integrating stratigraphic and dating information from different Last Glacial loess localities. *Palaeogeography, Palaeoclimatology, Palaeoecology 466*, 240–251.

Zöller, L. & Pernicka, E. 1989: A note on overcounting in alpha-counters and its elimination. *Ancient TL 7*, 11–14.

Supporting Information

Additional Supporting Information may be found in the online version of this article at http://www.boreas.dk.

Fig. S1. Lowest 2.5 m of the cleaned Hecklingen profile.

Fig. S2. Cleaned Hecklingen profile at a depth of ~7–5 m.

Fig. S3. Cleaned Hecklingen profile at a depth of ~5–2 m.

Fig. S4. Uppermost 3 m of the cleaned Hecklingen profile.

Fig. S5. Uppermost (left) and lowermost (right) parts of the cleaned Zilly section.

Fig. S6. Fading rates expressed as *g*-values (normalized to 2 days; Huntley & Lamothe 2001), as derived with the modified IRSL SAR protocol (see Table 2 in the main text) for the samples BT1535, BT1539 and BT1543.

Fig. S7. Class-wise and sample-wise explained variance of the grain-size data sets from Hecklingen (A) and Zilly (B), as derived from the application of the EMMAgeo program (Dietze *et al.* 2012; Dietze & Dietze 2016, 2019).

Fig. S8. Semi-generalized stratigraphy of the Hecklingen site (from Krauß *et al.* 2016) with classical main grain-size classes (clay, silt, sand) and the scores of the three loadings obtained by applying the EMMAgeo algorithm after Dietze *et al.* (2012) and Dietze & Dietze (2016, 2019).

Fig. S9. Semi-generalized stratigraphy of the Zilly site (from Krauß *et al.* 2016) with classical main grain-size classes (clay, silt, sand) an the scores of the three loadings obtained by applying the EMMAgeo algorithm after Dietze *et al.* (2012) and Dietze & Dietze (2016, 2019).

Table S1. Summary of fading rates measured for samples BT1535, BT1539 and BT1543 with the IRSL protocol outlined in Table 2. The shown *g*-values are normalized to a delay time of 2 days.

Data S1. Details of luminescence dating procedures.